GPS Imaging of Mantle Flow-Driven Uplift of the Apennines, Italy

William Charles Hammond[1] and Nicola D'Agostino[2]

[1]University of Nevada Reno
[2]Istituto Nazionale di Geofisica e Vulcanologia

November 21, 2022

Abstract

We use a newly updated GPS dataset and the GPS Imaging technique to show that the relief of the Apennines Mountain chain in Italy is currently increasing along its entire length by 1-2 mm/yr. We image positive uplift along the entire length of the Apennine crest including the northern Apennines, Calabria and northern Sicily. The maximum uplift rate is aligned with the topographic drainage divide, the greatest elevations and the zone of horizontal extension accommodating east-northeast translation of the Adriatic microplate relative to the Tyrrhenian Basin. Uplift occurs in a 100 - 150 km wide zone with a profile similar to the long wavelength topography, but not to shorter wavelength topography generated by active faulting and erosion. A zone of lower amplitude uplift aligns with the restive volcanic fields and high geothermal potential west of the Apennines, e.g., at Campi Flegrei, Alban Hills, and Monte Amiata-Larderello. Several factors including consistency of the geodetic rate with geologic uplift rates, and incompatibility with transient hydrological or earthquake cycle effects imply that it is a long-lived feature. Uplift occurs despite that the expected consequence of extension is crustal thinning and subsidence, suggesting a causal relationship between gravitational forces and active extension. Anomalies in gravity and upper mantle seismic velocity suggest that elevation gain is driven by forces originating in the mantle. We use these observations to address the hypothesis that these forces result from upward flow of asthenosphere beneath the Apennines, although the spatial and temporal scale of the mantle circulation is unclear.

Supplementary Table S1. List of networks and internet locations from which we obtained RINEX data

Network Abbreviation	Data Source
ABRUZZO	http://gnssnet.regione.abruzzo.it
ALBANIA	http://geo.edu.al/gps/obs
CALABRIA	http://gpscalabria.protezionecivilecalabria.it
CAMPANIA	http://gps.sit.regione.campania.it/indexvisual.php
DPC	http://www.protezionecivile.gov.it
EMILIA	http://www.gpsemiliaromagna.it
EUREF	http://www.epncb.oma.be
FREDNET	http://frednet.crs.inogs.it
FVG	http://gnss.regione.fvg.it/dati-GPS/default.jsp
GEODAF	http://geodaf.mt.asi.it
IGS	http://www.igs.org
ISPRA	http://www.isprambiente.gov.it
ITALPOS	http://it.smartnet-eu.com
LAZIO	http://gnss-regionelazio.dyndns.org
NETGEO	http://www.netgeo.it
OLG	ftp://olggps.oeaw.ac.at
PUGLIA	http://gps.sit.puglia.it
RENAG	http://webrenag.unice.fr
RGP	http://rgp.ign.fr
RING	http://ring.gm.ingv.it
SIGNAL	http://www.gu-signal.si
SOGEI	https://gnss.sogei.it
SONEL	http://www.sonel.org
UMBRIA	http://labtopo.ing.unipg.it/labtopo
UNAVCO	https://www.unavco.org
VENETO	http://retegnssveneto.cisas.unipd.it

Abbreviation for each network is used in second column of Table S2

GPS Imaging of Mantle Flow-Driven Uplift of the Apennines, Italy

William C. Hammond[1] and Nicola D'Agostino[2]

April 2020

1) Nevada Geodetic Laboratory
Nevada Bureau of Mines and Geology
University of Nevada, Reno
whammond@unr.edu

2) Istituto Nazionale di Geofisica e Vulcanologia
Osservatorio Nazionale Terremoti
Rome, Italy

Key Points:

• A newly updated GPS velocity field reveals uplift of 1-2 mm/yr along the entire length of the Apennines.

• The uplift is aligned with the location of active extension, high topography, seismicity, high gravity, and an upper mantle seismic anomaly.

• These correlations suggest that mantle upwelling contributes to the ongoing increase of elevation and focusing of extensional strain.

Short Title: GPS Imaging Apennine Uplift

Index Terms:
1240: Geodesy and Gravity: Satellite geodesy: results
1213: Geodesy and Gravity: Earth's interior: dynamics
8105: Tectonophysics: Continental margins: divergent
8121: Dynamics: convection currents, and mantle plumes

Abstract

We use a newly updated GPS dataset and the GPS Imaging technique to show that the relief of the Apennines Mountain chain in Italy is currently increasing along its entire length by 1-2 mm/yr. We image positive uplift along the entire length of the Apennine crest including the northern Apennines, Calabria and northern Sicily. The maximum uplift rate is aligned with the topographic drainage divide, the greatest elevations and the zone of horizontal extension accommodating east-northeast translation of the Adriatic microplate relative to the Tyrrhenian Basin. Uplift occurs in a 100 - 150 km wide zone with a profile similar to the long wavelength topography, but not to shorter wavelength topography generated by active faulting and erosion. A zone of lower amplitude uplift aligns with the restive volcanic fields and high geothermal potential west of the Apennines, e.g., at Campi Flegrei, Alban Hills, and Monte Amiata-Larderello. Several factors including consistency of the geodetic rate with geologic uplift rates, and incompatibility with transient hydrological or earthquake cycle effects imply that it is a long-lived feature. Uplift occurs despite that the expected consequence of extension is crustal thinning and subsidence, suggesting a causal relationship between gravitational forces and active extension. Anomalies in gravity and upper mantle seismic velocity suggest that elevation gain is driven by forces originating in the mantle. We use these observations to address the hypothesis that these forces result from upward flow of asthenosphere beneath the Apennines, although the spatial and temporal scale of the mantle circulation is unclear.

Plain Language Summary

We use a newly generated compilation of high-precision geodetic data from hundreds of GPS stations to generate a map of the active uplift that shows the Apennine Mountains of peninsular

Italy currently rising by 1-2 mm/yr. The dataset has greater precision, accuracy and coverage than those previously available. Our analysis focuses on the spatial patterns of the inferred uplift and compares the signals to those in gravity, topography, geomorphic, geologic, and seismic data. We use the data to show that the uplift is representative of solid Earth processes active over geologically relevant periods of time, possibly millions of years, and is related to vertical flow of the Earth's mantle beneath Italy. This active geodynamic process is related to tectonic crustal extension across the Tyrrhenian/Adriatic plate boundary, the evolution of the drainage network, and the presence of hazards from earthquake in the Apennines.

1. Introduction

The topography of Italy south of the Po Plain is dominated by the Apennine mountain chain that extends along the length of the Peninsula from the western Alps in the north to Calabria in the south (Figure 1). The length of the chain is about 500 km, elongated in the NW–SE direction and approximately 100 km wide, occupying about half the width of the Peninsula. The region lies within a plate boundary setting of active north-south convergence between the Eurasian and Nubian plates, where complex Mediterranean tectonics include multiple loci of subduction, extension, and transform tectonics (Faccenna et al., 2014a). The Apennines were most likely formed during Neogene southwest directed subduction of the Adriatic lithosphere beneath the Tyrrhenian lithosphere (Patacca and Scandone, 1989; Serri et al., 1993; Royden et al, 1987) and possibly associated with rollback of the subducting slab that pulled the trench toward the Adriatic (Malinverno and Ryan, 1986). Early Quaternary time saw a marked change in conditions for this plate boundary's dynamic balance, indicated in a record of regional doming of the Apennines and unflexing of the Adriatic plate (Cinque et al., 1993; D'Agostino et al., 2001b;

Kruse and Royden, 1994). On the Adriatic side of the Apennines this process interacted with Quaternary eustatic sea level fluctuations and caused the basinward migration of shallow marine deposits, forming an overall prograding system (Ori et al., 1993; Pizzi, 2003). Starting at 2-3 Ma basins developed within central Italy (Martini & Sagri, 1993) coincident with an extensional phase of the axial part of the Apennines that continues to the present day (Cosentino et al., 2017).

The geological and geomorphological observations, summarized in D'Agostino et al. (2001b), suggest a general doming of the Italian peninsula during the Quaternary on a wavelength larger than 150-200 km. Today, the locus of extension, normal faulting, and seismicity, which drive contemporary generation of local relief, occupy the region with highest elevations and drainage divide of the Apennines (Bartolini et al., 2003; D'Agostino et al., 2001b, 2011). This deformation pattern is consistent with contemporary kinematics of the Adriatic, Tyrrhenian, Nubian, and Eurasia plate motions in the central Mediterranean, which have been charted using geodetic results from regional GPS networks (Bennett et al., 2012; D'Agostino et al., 2008; Devoti et al., 2011; Kreemer et al., 2014; Serpelloni et al., 2005). These studies tend to broadly agree on the overall patterns of translation of the Adriatic to the northeast with respect to Eurasia and the Tyrrhenian lithosphere at a rate of 3-5 mm/yr, driving a zone of extension across the Apennines (D'Agostino, 2014). Vertical geodetic signals are detectible and correlated with topography, but are more difficult to relate directly to geodynamic processes driving elevation growth because the signals have had high noise and contributions from transients that do not necessarily reflect long-term topographic evolution (Bennett et al., 2012; Cenni et al., 2013; D'Anastasio et al., 2006; Devoti et al., 2011; Serpelloni et al, 2013; Silverii et al., 2016). These studies seem to agree, however, that the shallow processes driving seismicity and strain rates in the crust are related to the current configuration of the plate boundary, and are responsible for much of the regional seismic hazard (Stucchi et al., 2011).

The evolution of Apennine topography has also been connected to upper mantle flow. For instance, the relationship between gravity signals and topography through the analysis of admittance, in addition to the presence of uplifted shorelines, suggest a long-term contribution of the mantle to regional uplift (D'Agostino et al., 2001b). The role of active faulting in river drainage capture suggests a contribution from a broad regional uplift of the lithosphere (Geurts et al., 2018). The presence of residual topography in the central Apennines is consistent with the dynamic support from the uppermost mantle, suggesting upward flow (Faccenna et al., 2014b). Mantle structure is constrained by seismic tomography which reveals a high wave speed anomaly whose depth range and shape suggest the presence of a sinking slab (e.g., Faccenna et al., 2014b; Giacomuzzi et al, 2011). However, issues of image resolution and coverage still exist, making it difficult to determine the scale of mantle circulation, degree of continuity of the slab, and degree to which it is dynamically connected the upper plate.

Here we use geodetic constraints to show that the uplift of the Apennines extends along the entire length of the chain, increasing long wavelength relief by 1-2 mm/yr. These results are based on a new GPS velocity solution that employs a larger number of stations and is developed using the latest processing models and standards, referred to the IGS14 global reference frame. We show that there is a very close alignment between the area of uplift and active strain rates, seismicity and modern topographic drainage divide. These relations point to an intimate relationship between active crustal uplift, mantle flow, crustal extension and landscape development of the Apennines, suggesting that they share a common dynamic source.

2. Data

2.1 GPS Data Processing and Filtering

We use GPS data collected from multiple high precision GPS networks that comprise the data holdings of the Osservatorio Nazionale Terremoti (ONT), Instituto Nazionale di Geofisica e Vulcanologia (INGV). The ONT-INGV data come from a set of 1648 stations whose geographic distribution is focused on Italy, but whose total coverage extends from latitude -40˚ to 79˚, and longitude -69˚ to 129˚. The individual networks and links from which we obtained data are listed in Supplementary Table S1. Data from this collection have been processed using the Gipsy software (v. 6.3) from the Jet Propulsion Laboratory (JPL) and associated JPL data products (satellite orbits, clocks, Earth orientation parameters) to solve for daily (24 hour) positions in a daily free-network, satellite-based reference frame. For the ensuing analyses we realized two versions of station time series in the ITRF2014 reference frame (Altamimi et al., 2016). The first realization used the global JPL x-files to transform daily positions in the free-network, satellite-based frame to the ITRF2014 frame. The Helmert parameters in the JPL x-files are derived from a global distribution of stations and are thus unlikely to be affected by hydrological loading at regional scale. Because we are primarily interested with relative horizontal and vertical motions across the Apennines we realized an additional version of the ITRF2014 time series applying a continental-scale, common-mode filtering (Wdowinski et al., 1997) to reduce the impact of daily noise in the network solution. This filtering is realized by calculating the Cartesian coordinates and velocities from the "global" ITRF2014 daily solutions for 132 stations in and around the Eurasia plate selected by specific quality criteria. This solution is aligned in origin and scale with ITRF2014 but it is implemented to have no-net rotation with respect to the stable interior of the Eurasian plate, by subtracting a rigid rotation estimated from a 32-station core subset. This reference frame realization method transforms the station time series into a plate-fixed frame and effectively applies a continental-scale spatial filter to the station coordinates, leading to a reduction of the common-mode errors (Wdowinski et al., 1997), and to an increase of the signal-to-noise ratio. The first set of time series was used to calculate the effect of hydrological loading and its possible effects on the uplift rate (section 5.1) whereas the second set was used to estimate the horizontal and vertical displacement rates with MIDAS (section 2.2).

2.2 MIDAS Velocities

To estimate rates of motion for each station we applied the robust MIDAS trend estimator (Blewitt et al., 2016) to obtain the three-component modal velocity from the filtered time series. MIDAS is a non-parametric statistical method that estimates the time series trend by computing the median of rates made from all pairs of data with a time difference of about 1 year (Theil, 1950; Sen, 1968). The algorithm is generally, by design, blind to seasonality, outliers, undocumented steps and heteroscadasticity. In blind tests MIDAS has been shown to be very accurate, to produce realistic uncertainties, and also has short computation time and so is efficient to use on large datasets.

2.2.1 Time Series Discontinuities

While MIDAS is generally robust, even in the presence of (even unknown) discontinuities in a time series, it can be used with an option where data pairs crossing times of known potential steps are omitted. This further ensures that the analysis is not impacted by the presence of equipment or earthquake related steps in the time series. We used this option in conjunction with a database of known equipment and earthquake events. The equipment discontinuity event database is generated from IGS site logs and RINEX data headers whose metadata indicate when a receiver or antenna type or model changed. It is publicly available at http://geodesy.unr.edu/NGLStationPages/steps.txt (Blewitt et al., 2018). We consider a potential earthquake-related step when its magnitude has M>5.5, occurred within a station's observation time interval, and was located within an empirically derived distance between event epicenter and station, defined by $10^{(M/2\ -\ 0.8)}$ degrees, where M is magnitude. For many of the events there was no visible offset of the time series, which can happen if the earthquake is near the distance limit or the equipment change was between similar devices. In practice inclusion or omission of these steps has a significant impact on only a very small fraction of station velocities. In our dataset 97%(99%) of the vertical(east) MIDAS velocities change by less than 1 mm/yr when including steps information. This stability is attributable to the limited number and small size of actual discontinuities in the dataset, and to the robustness MIDAS has when solving for trends in the presence of steps. Because the next stage of the imaging analysis described below is itself also robust to velocity noise, considering the step times has almost no impact on the final outcome of the analysis. In what follows we show results for the case where the steps are included.

2.2.2 Statistics and Uncertainties

In Figure 2 we show histograms for the subset of stations having location inside the geographic bounds of Figure 1, at least 2.5 years of position time series duration, and MIDAS vertical velocity uncertainty of less than 2 mm/yr. There are 648 GPS stations meeting these criteria. Stations, networks, locations and velocities are listed by name in Supplemental Table 2. The histograms of time series duration indicate that most of the stations have as much as 19.4 years, with a median of 8.7 years of data. Thus, they are sensitive primarily to deformation that occurred over the last two decades. Time series completeness is skewed heavily towards 100%, with a median completeness of 89.0%. However, some high quality stations with more sparse occupation schedules where included, though only 2.5% (15%) of the stations have completeness less than 50% (75%). The histograms of vertical velocity uncertainty show that the exclusion of stations with uncertainty greater than 2 mm/yr effects a small number of stations, and that the vast majority of horizontal rate uncertainties are less than 0.5 mm/yr.

2.2.3. Correction for Glacial Isostatic Adjustment

Following the Last Glacial Maximum (LGM) the loss of continental ice sheets changed the surface loads of northern Europe, resulting in an ongoing contemporary Earth surface motion in all three components across the Mediterranean (Haskell, 1935; Vening Meinesz, 1937). These movements extend across the Mediterranean and must be accounted for if we wish to focus on surface motion attributable to the more local to regional Apennine tectonics and mantle dynamics. Serpelloni et al., (2013) discussed similarities and differences between the predictions from two recent independent models, ICE5G (VM2) (Peltier, 2004) and the model of Lambeck et al., (1998) in the Mediterranean region. They found that while the models differ slightly in terms of vertical rates and the steepness of their gradients from the European platform north of the Alps to the central Mediterranean, they agree that the signal along the Italian Peninsula is predicted to be subsidence, dipping approximately linearly towards faster subsidence rates between -0.3 and -1.0 mm/yr to the southwest.

In following sections we discuss the pattern in uplift rate that we find for the Italian Peninsula. The pattern we observe is not similar to the predicted ramp in subsidence from GIA, and thus the GIA process is not a likely explanation for these signals. However, GIA can affect all the stations similarly, and so give the impression of overall subsidence and obscure the signals of active relief generation that increases and decreases elevations near the Apennines. As mentioned above we focus on signals attributable to tectonics and mantle dynamics on Italy so we correct the velocities for GIA by subtracting the predictions of the more recent ICE-6G model (Peltier et al., 2015) interpolated to the GPS stations used in our analysis (Supplementary Figure 1). We acknowledge that the GIA model predictions have their own uncertainties and that residual signals from the GIA process may remain. However, because the ice depocenter was distant to the north, residual GIA signals can be approximated as a gentle ramp across Italy on the order of a few tenths of a mm/yr or less. The ICE-6G model has less rapid Mediterranean subsidence compared to the model of Lambeck et al., (1998), so correcting with the latter model would result in faster uplift than we show below. The median vertical rate of the filtered IGS14 rates after correction for the effects of GIA is -0.05 mm/yr, and the median vertical rate in the image is -0.17 mm/yr, which are both statistically indistinguishable from zero. This suggest that the correction removed long wavelength signal that is not related to local tectonic activity.

3. Methods

3.1. GPS Imaging

To robustly estimate the three-component velocity fields we use GPS Imaging which includes the determination of time series trends using MIDAS (Hammond et al., 2016). The imaging uses a weighted-median strategy which makes it effective for identifying the part of a spatially variable signal that is consistent across multiple stations. The technique estimates field values on a discrete regular grid points using Delaunay triangulation of the GPS network with an ad hoc inclusion of the grid point. Each grid point estimate is based only on the values at neighboring stations within the ad hoc triangulation, which is repeated anew for every point. The geographic resolution of the imaging is limited only by the station spacing. The estimated field is insensitive to outlying data of arbitrary magnitude as long as they are isolated, i.e., not corroborated by neighboring data. Therefore, the stability and appearance of the field is derived from consensus among the data and not from averaging or classical smoothing through any least-squares formalism.

The medians are weighted by the value of a spatial structure function (SSF) derived from the data, divided by the data uncertainty (Hammond et al., 2016). Our derivation of the SSF is provided in the Supplementary text. In practice the results of the imaging are insensitive to the details of the SSF when the network is dense, but has more impact at grid points where station density is sparse or asymmetric on either side of a grid point. For both vertical and horizontal component imaging we apply a preliminary median spatial filtering of the velocities to remove outliers, and then interpolate with GPS Imaging to obtain a gridded field. We perform the imaging using all velocities from stations located within a latitude/longitude bounded box that superscribes the area of Figure 1 by at least one degree. This prevents undesirable edge effects in the imaging that could occur if we exclude stations immediately outside the model domain.

Finally, to further enhance the robustness of the estimated field, we repeat the imaging 20 times, using a randomly selected 75% of the velocities each time, and for every pixel we take the median value of the images. This step further reduces the ability of individual GPS velocities to impact the result.

3.2. Uncertainty in GPS Imaging

The ability that GPS Imaging has to resolve geographic patterns of uplift and deformation depends on the size of the signals compared to the uncertainties, in addition to the density and location of stations in the GPS network. The velocities at each pixel are constrained by observations at multiple locations and thus have uncertainties less than those at at individual stations. For example, the median vertical velocity uncertainty at the stations derived from MIDAS is 0.65 mm/yr, while the median formal uncertainty of vertical rates estimated at grid points in the images is ~0.28 mm/yr. We assess the ability of GPS Imaging to resolve the rates and patterns of uplift across the Apennines by performing a sequence of tests that take the actual station locations into account (see Supplementary Materials). The results of these test show that the main uplift signal along the length of the Apennines and continuing into Calabria and northern Sicily are consistent in all tested subsets of the data. We tested cases by choosing subsets of time periods, different halves of the stations selected quasi-randomly, and different time series duration cutoff thresholds, all arriving at essentially similar results. The stability of the derived field is attributable to many factors, including extensive GPS network coverage, with improvements in the number, geographic density and redundancy of stations in the network, duration of time series resulting in low rate uncertainties, improvement in GPS data processing, reference frame stability, and additionally the robustness of our imaging methods. We conclude that having a broad and dense distribution of long duration time series (>10 years data) is essential for resolving the signals of geographically coherent vertical uplift in the Apennines (see Supplement). The vertical rate field we obtained is shown in Figure 3.

4. Results

4.1. GPS Imaging Apennine Uplift

The vertical rate field along the Italian Peninsula indicates upward motion of the entire Apennine chain (Figure 3). Positive uplift extends continuously from the northern Apennines, adjacent to the Po Plain following a zone that extends uninterrupted to the southern tip of Calabria in the south. Across the Strait of Messina the uplift continues into Sicily. Uplift in northeast Sicily is clearly enhanced by time-variable magmatic inflation of Mount Etna (e.g., Bonaccorso et al., 2015) and so is likely not representative of processes effecting the rest of the Apennines. However, the uplift signal exists in GPS stations in western Sicily as well, continuing to west of Palermo, with an uplift rate similar to the rest of the Apennines.

North of the Apennines, on the Po Plain subsidence clearly dominates the vertical rate field between the northern Apennines and the Alps. This is one of the largest and most robust parts of the signal in the imaging. Station coverage here is strong and the magnitude of the signal is greater than the rate uncertainties and greater than the signal in the Apennines. The median rate of subsidence is near -4 mm/yr but is greatest toward the Adriatic coast and municipality of Venice. This signal has been attributed to processes such as sediment compaction, aquifer depletion, and geodynamic subsidence and so the total uplift is likely attributable to a combination of pumping, geologic, tectonic and mantle driven processes (Bennett et al., 2012; Bock et al., 2012; Carminati et al., 2003; Devoti et al., 2011; Gatto and Carbognin, 1981;

Serpelloni et al., 2013; Tosi et al., 2002). The GPS Imaging result shows a transition between subsidence in the Po Plain and uplift in the Northern Apennines (up to ~1 mm/yr) that very closely follows the topographic transition. Uplift in the Emilia Romagna section of the Northernmost Apennines is subdued, near 0 mm/yr, but is upward relative to the Po Plain to the northeast and to the Ligurian Coast near Pisa and Viareggio to the southwest.

To show details of the Apennine uplift signal we create three 100 km-wide profiles of vertical velocity along the Italian Peninsula drawn normal to the average trend of the Apennine chain (Figure 4). These show that the uplift generally has a peak near the topographic drainage divide. However, the peak in velocity is wide and not limited to the location of the divide. The uplift is a broad doming with wavelength between 100 and 150 km, wide enough to encompass the width of the high Apennine elevations. For reference on the profiles we plot the location of an Early Pleistocene shoreline that has been uplifted to between 220 and 480 meters above sea level (D'Agostino et al., 2001b; Mancini et al., 2007), its location is shown on Figure 1. While uncertainties and disagreement about the age of the shoreline exist (Mancini et al., 2007; Cosentino and Fubelli, 2008), it is likely that the movement started at 2.5 to 1.5 Ma, suggesting an uplift rate in the range 0.1-0.3 mm/yr. Conservatively accounting for uncertainty we plot a bar on Figure 4 that shows a range of uplift rate from 0 to 0.5 mm/yr at the location of the shoreline. Comparison between the GPS measured uplift and this long-term uplift rate indicate agreement to within this level of uncertainty, with the northern profile on the high range and the central profile on the lower range.

The flanks of the uplift, near the Tyrrhenian and Adriatic coasts at the SW and NE ends of all the profiles, have rates that are near zero or downward (Figure 4). An embayment of subsidence, with rates between -0.5 and -1.0 mm/yr primarily impacts the NE end of the northern and central profiles between the Apennine crest and the Adriatic coast (Figure 3). This zone lies within the Apennine fold and thrust belt, a structural remnant of convergence associated with west directed subduction of Adriatic lithosphere and Neogene formation of the Apennines (e.g. Kligfield, 1979; Elter et al., 2003; Pace et al., 2015; Patacca and Scadone, 1989).

West of the drainage divide the vertical rate image in Figure 3 shows three equant anomalies that lie near restive volcanic complexes. These systems are Campo Flegrei to the south, the Alban Hills 20 km southeast of Rome, and an area in Tuscany that roughly includes the Monte Amiata and Larderello geothermal fields. All three of these areas display some characteristics of active magmatic systems. The Monte Amiata-Larderello area has an active geothermal field (Gianelli et al., 1997; Batini et al., 2003), the Alban Hills caldera has minor earthquakes and was the location of a major eruption at 36 ka (Cecconi et al., 2010; Freda et al., 2006), and the Campi Flegrei near Naples has experienced large uplift over 10k years and contemporary unrest in the 20th century (Isaia et al., 2009). Uplift signals from the Monte Amiata-Larderello and the Alban Hills anomalies appear on our northern and central GPS profiles, respectively, but the Campi Flegrei anomaly lies too far north of the southern profile and so does not appear (Figure 4). On the SW side of the northern profile the anomaly reaches 1 mm/yr uplift and rises above the anomaly that is centered on the drainage divide to the east. The Alban Hills has a somewhat lower intensity anomaly (< 1 mm/yr) on a second hump on the west side of the central profile. The fact that these anomalies are associated with volcanic systems may indicate that they are not as long lived as the anomalies near the central Apennines that we attribute to tectonic uplift. This may explain why the uplifted Early Pleistocene shorelines in Figure 4AB appear east of the current uplift anomalies. On the other hand the geodetic uplift signal in Tuscany spatially corresponds with the area of uplifted Plio-Quaternary sediments along the Tyrrhenian side of the Apennines (Marinelli et al., 1993) with the main peaks reached at Larderello and Monte Amiata geothermal fields for both the long-term and geodetic signals (Figure 5). This correspondence may suggests that the magmatic intrusions responsible for the Larderello and Monte Amiata geothermal fields (Gianelli et al., 1997; Batini et al., 2003) are still active.

To the south stations on the Aeolian Islands in the Mediterranean Sea north of Sicily experience downward motion overall, but are also effected by volcanic deformation of e.g., the islands of Volcano, Stromboli, etc. (e.g., Cintorrino et al., 2019). While it is possible with GPS Imaging to interpolate the vertical field into areas covered by the Mediterranean sea, we have chosen to omit from the images all areas covered by the sea since it is generally not well sampled with GPS stations that have not been effected by active volcanic deformation. However, we do include island data in the imaging of onshore vertical land motion. The masking of the sea-covered areas could lead to some bias in the impression given by the inferred uplift pattern. However, as shown above, the Apennine uplift consistently tends to zero on the Tyrrhenian and Adriatic coasts indicating that the vertical rate anomaly is focused on the Apennine crest.

4.2. GPS Imaging Horizontal Velocity

Previous studies of horizontal GPS velocities have shown the general pattern and rates of active extension across the Apennine chain (e.g., Bennett et al., 2012; D'Agostino et al., 2001a; 2011;

D'Agostino, 2014; Devoti et al., 2011; Serpelloni et al., 2005). We here apply GPS Imaging to the east and north component MIDAS velocities to obtain a gridded version of the velocity field that can be compared to the vertical rate field. For the horizontal imaging we use the same SSF that we derived for the vertical velocities in order to maintain consistency in the signal wavelengths preserved in the imaging. In Figure 6A we present the MIDAS horizontal velocities and in Figure 6B the gridded version obtained with GPS Imaging decimated by a factor of 2 from the underlying node density for visual clarity.

We find, similar to previous studies, ~3 mm/yr of near-uniaxial spreading in a zone of extension that is centered on the Apennine chain. These steepest velocity gradients are focused directly on the drainage divide (Figure 6). This is clearer in the profiles of horizontal magnitude of velocity (Figure 7) that have the same locations as the profiles in Figure 4. These show that the steepest velocity gradient delineates a zone of accommodation that is 25 to 40 km wide and almost always within the range of along-profile distances defined by the drainage divide.

There is sparse distribution of velocities on the Dalmatian coast and Dinaride Alps east of the Adriatic, but given the greater number of very consistent velocities on the Adriatic coast of Italy, there are enough to allow preliminary reconstruction of the velocity field across the Adriatic. The velocity gradients are gentle and describe a northeast movement with azimuths that vary with latitude up the Adriatic Sea. The changes in gradients may be attributable to lack of rigidity and distinct kinematics between the northern and southern Adriatic (D'Agostino et al., 2008; Oldow et al., 2002).

4.3. GPS Imaging of Horizontal Strain Rate

From the gridded horizontal velocity field we estimate the velocity gradients attributable to crustal strain rates. Deriving strain rates from the gridded field improves geographic balance in the strain rate solution and reduces the tendency for the solution to work more heavily to satisfy data where stations are densely spaced. The technique evaluates strain at every grid point in the model, using a Gaussian weighting function to more heavily weight stations that are closer to each evaluation point (Hammond et al., 2019). Choosing an optimal value for the width of the weighting function is non-unique. We select the width w = 8 km, which is chosen because it is low enough so that model misfit is low, and large enough to suppress artifacts (see supplemental materials). We use the relations of Savage et al., (2001) to solve for components of rotation and strain rate on the surface of a sphere. A map of the dilatational strain rate (the sum of the two principal strain rates e_1 and e_2) is shown in Figure 8. In our convention negative values are contraction and positive values are extension (area growth). We focus on the dilatational strain rate because the Apennine deformation zone is in uniaxial extension, a condition where $\dot{e}_1 > 0$ and $\dot{e}_2 \approx 0$, so dilatation corresponds to the uniaxial strain rate.

The map shows a robust stripe of high strain rates (>50 x 10^{-9}/yr) in a zone corresponding to the location of the Apennine drainage divide (Figure 8) and M > 6 earthquakes (Rovida et al. 2019). Similar to the uplift, the strain extends along the entire length of the Apennine chain, from the Po Plain to southern tip of Calabria. Also similar to the uplift, the strain continues across the straight of Messina, passes through the active zone affected by Etna volcano, and continues into northern Sicily. Also, west of the main axis of strain rate there is a secondary stripe of active strain that aligns with the secondary zone of uplift, which is occupied by restive volcanic zones discussed above and shown in Figure 3. The strain is plotted on the profiles (Figure 7) showing that the secondary zone of strain to the west has lower amplitude, and is aligned with the secondary uplift. In the northern and central profiles the western secondary zone of uplift is the greater of the two, but the strain rates are greater near the uplift focused on the Apennine drainage divide. This suggests that the Apennines are the primary locus of uplift and strain, and that the western uplift, corresponding to weaker crustal strain is enhanced by the magmatic systems beneath the scattered volcanic systems of western Italy.

5. Ruling out Transient Processes

5.1. Hydrological Loading Effects?

Recent geodetic studies of mountain uplift has found that it may in some cases be driven primarily or in part by short term transient hydrological surface loads that vary seasonally (e.g., Amos et al., 2014; Argus et al., 2014; Chanard et al., 2014; Fu and Freymueller, 2012; Fu et al., 2015; Heki, 2001) or have trends driven by multi-annual to decadal changes in surface water content (Amos et al., 2014; Argus et al., 2017; Chen et al., 2018; Fu and Freymueller, 2012; Hammond et al., 2016) and not necessarily related to long-term development of the topography. A previous study in the Southern Apennines focused on the hydrological contribution to seasonal and multi-annual transient deformations, showing that upward motion averaged by multiple stations is inversely correlated with Equivalent Water Height signal from GRACE (Silverii et al., 2016). This motivates us to consider if a drying and unloading trend, whose temporal scale is longer than the multi-annual signal (4-5 years) observed by Silverii et al. (2016) could explain the observed uplift signals in the Apennines.

To address this question we consider data from the GRACE satellite mission which measures the Earth's time-variable gravity field, and is sensitive to the changing distribution of surface water which can cause vertical motions via loading. Data from GRACE collected from 2003 to 2016, overlaps the time of collection of our GPS data. We considered the JPL (Watkins et al., 2015; Wiese et al., 2016) and GSFC solutions (Luthcke et al., 2013) accessed via the mascon visualization tool developed by the University of Colorado (https://ccar.colorado.edu/grace/). GRACE spatial resolution is typically on the order of 300-400 km, larger than the width of the Apennines (~200 km). Thus, all GRACE mascons intersect one of the Adriatic, Tyrrhenian or Ionian seas to some degree. As a result the solutions may be partially influenced by the changing gravity owing to Mediterranean Sea level changes, in addition to the terrestrial water storage. These leakage errors are addressed specifically in the JPL solution, where an attempt was made to partition the gravity signal into sea and land components (Watkins et al., 2015). The GSFC mascons are smaller so overlap less with the sea, but may be affected by correlation between adjacent mascons, and associated errors.

However, while these considerations indicate uncertainties in the GRACE products, we observe that the gravity trends for all the mascons near the Apennines are positive suggesting mass gain over time. We illustrate this for an example equivalent water height (EWH) time series solution for GSFC mascon #5339 that covers Naples and a large part of southern Italy (Figure 9A), which has a trend of 0.41 cm/yr. We compare this to a stack of vertical time series for GPS stations included within the area defined by the mascon #5339 characterized by low scatter, and step-free time series. To avoid suppression of loading signal from our filtering of common-mode signal, for this analysis we used IGS14 position time series obtained directly from the global transformation parameters (x-files) provided by JPL (see section 2.1). The stack of these GPS vertical time series (Figure 9B) has an upward trend of 0.58 mm/yr modulated by seasonal and multi-annual signals whose source is likely hydrological surface loading (Silverii et al., 2016). Aside from their trends the structure of the GRACE and stacked GPS time series in their seasonality and multi-annual patterns are, in fact, similar. This can be seen in by comparing detrended GPS vertical and GRACE time series (Figure 9C). Also we show a scatter plot of the monthly GRACE value (in units of cm EWH) against the monthly median GPS value (in mm vertical position) (inset in Figure 9C). From these data we calculate a regression between the two variables which has a slope of -0.45 mm/cm which can be considered a linear transfer function between the hydrological forcing EWH (input) and the resulting vertical motion (output). Assuming that the observed trend in the stacked GPS time series is exclusively caused by hydrological forcing, this linear transfer function can be used to estimate the predicted EWH trend. In other words we use the observed elastic response of the Earth surface at seasonal and multi-annual scales to predict the EWH trend expected in the hypothesis of hydrological unloading. The resulting predicted EWH trend expected from the GPS data has a negative slope (0.58 mm/yr/-0.45 mm/cm = -1.3 cm/yr blue in Figure 9A) in contrast to the actual GRACE data which has a positive slope. We conclude from this simple test that, while the GPS and GRACE signals have very similar structures, and are likely measuring the same seasonal to multiannual surface water variability, they differ in their trends and thus are measuring different long-term processes.

This result is representative of other mascons covering the Apennines that show trends of between 1 to 5 mm/yr of increasing EWH over the period of observation (the range considers differences between, and spatial variation of GSFC and JPL solutions). These trends are near the level of uncertainties, but are consistently positive over the Apennines. Thus, despite the uncertainties and resolution issues involved in the GRACE results, they do not seem to support the occurrence of a drying trend that could explain the uplift. The GPS data seem to have trends that are not predicted by GRACE EWH estimates and thus likely have a different origin.

One possible interpretation of these observations is that increasing terrestrial water storage explains the GRACE data, but is not sufficient to provide enough loading to overcome mantle flow driven Apennine uplift. However, another possibility is that the GRACE signal is in whole, or in part, caused by an increase in mass associated with the uplift rather than surface hydrology. A mass increase would be observed, for example, if vertical mantle flow-related uplift was accompanied by horizontal mantle flowing inward to the asthenosphere beneath the Apennines, this would imply an increase in the length of the vertical mantle column to support the rising elevation. Moreover, owing to the greater density of mantle rocks compared to water, uplift from mantle flow will be over 3 times as effective in creating an EWH signal. Below we discuss our estimate of vertical mantle flow that is near 2 mm/yr, which is consistent with GRACE trends we observe of 0.4 cm/yr trend in EWH (Figure 9A). In this interpretation the mass gain seen by GRACE is not attributable to water, but to the increase in the amount of mantle rock mass beneath the satellite.

5.2. GPS Velocity Variability

In the discussion that follows we attribute the uplift imaged in Figure 3 to processes at work in the lithosphere and upper mantle. The scale of these processes suggest that, like plate tectonics, they proceed steadily over the periods of time we observe with GPS. We do not expect that uplift derived from mantle flow will vary substantially over a few years time. Thus the time variability of GPS velocity is one characteristic that can indicate when GPS data are not representative of movements associated with geodynamic processes that persist over long periods, possibly millions of years.

To assess the time variability of the uplift field we compute for each vertical GPS time series an index based on the MIDAS algorithm (Blewitt et al, 2016). For each time series we take 2-year long sub-intervals and compute the MIDAS rate for each interval. We start with the first 2 years of the time series, then select a new interval by shifting the window forward in time by one month, and repeat the process until the window extends beyond the end of the time series. The 2-year window size is selected because it is long enough to include enough data pairs separated by one year to compute the MIDAS rate, yet short enough so that many rate samples can be generated for the time series in our dataset. The result is a time series of MIDAS velocity for the station which indicates how the rate changed over the period of observation. This variability index is insensitive to outliers and seasonal periodicity because MIDAS rates are computed from pairs of data separated by one-year duration. Hence the index represents a robust measure of *non-seasonal variability* (NSV) in velocity. To compute the index we take the median absolute deviation (MAD) of the values in the velocity time series:

$$V_{u,NSV} = MAD(V_{MIDAS}([t_i - 1.0, t_i + 1.0])) \qquad (1)$$

which has units of mm/yr. Here V_{MIDAS} is the MIDAS velocity obtained from the interval of vertical component time series data over the 2 year interval [t_i - 1.0, t_i + 1.0] which is centered on t_i. Using the MAD (as opposed to the standard deviation) in (1) adds an additional layer of robustness since it is less sensitive to outlier rates that could be present in the velocity time series. Stations with complicated vertical motion history will have larger $V_{u,NSV}$, while stations with very linear trends have low $V_{u,NSV}$. A histogram of $V_{u,NSV}$ indicates the center, body and range in the distribution of $V_{u,NSV}$ values, 75% of which are less than 1.8 mm/yr (Figure 10A). A histogram of $V_{u,NSV}$ normalized by the uncertainty of the MIDAS rate for the full time series (Figure 10B) indicates that 34% of have $V_{u,NSV}/\sigma_{Vu}$ values greater than 2, suggesting that for this minority of stations the time variability is significant.

To test whether any important signals in uplift map in Figure 3 could be driven by time-variable uplift processes we repeat the imaging using only vertical rates from GPS stations that have V_{NSV} less than the median variability (1.8 mm/yr). This is similar to the other tests of robustness in which we repeated the imaging while omitting half the data, as presented in the supplemental materials. The result (Figure 10C) shows that the imaged uplift rate is very similar to the image made using all of the data, with the same major domains and rates of uplift and subsidence. While individual stations can have high values of $V_{u,NSV}$, those stations tend to be isolated and their impact is reduced by the robust imaging. Thus, the pattern of vertical land motion is supported by the least time-variable rate data.

5.3. Earthquake Cycle Effects?

The Apennines are one of the most productive earthquake regions in Italy and home of some of the largest and most damaging events. Maps of earthquake epicenters (Rovida et al., 2019) and hazard (Stucchi et al., 2011) show a strong correlation to the zone of uplift, but this is because the uplift is correlated with the active plate boundary deformation, not because the earthquakes or their aftershocks, or subsequent postseismic deformation, directly causes uplift of Earth surface. However, it has been shown that in extensional tectonic environments large earthquakes (e.g., M7 and above) can exhibit post-seismic viscoelastic uplift or strain that can last for decades (e.g., Gourmelen and Amelung, 2005; Reilinger, 1986). This deformation decays over time at a rate that depends on the elastic and viscoelastic properties of the crust and mantle, and on the postseismic process at play. Thus it may be reasonable to consider the question of whether the observed uplift could reflect a cumulative plate boundary-scale postseismic deformation having contributions from the many normal faults in the Apennines (Riguzzi et al., 2013).

We argue that this is unlikely. One argument is that the main signal generated by recent Apennine earthquakes is postseismic subsidence rather than uplift. For example, subsidence was observed for the L'Aquila event in 2009 (Albano et al., 2015; Cheloni et al., 2014; D'Agostino et al., 2012) and for the similar Norcia sequence in 2016 (Cheloni et al., 2017). Second, even if postseismic uplift occurs, e.g., as has been observed for multiple large extensional events in the Basin and Range (Gourmelen and Amelung, 2005; Reilinger, 1986), it is statistically improbable that postseismic uplift would be currently present along the entire Apennine chain. If, for example, measurable postseismic vertical motion is detectible over the fault for 100 years after the event, and recurrence intervals are ~2000 years (Galli et al., 2008), each fault would only exhibit postseismic uplift about 5% of the time. In reality recurrence intervals could be much longer, e.g., Galandini and Galli, (2003) found recurrence intervals of 4690 and 7570 years for the Mt. Vettore Fault and Laga Mtn. Fault respectively. Also, relaxation times may be much shorter, e.g., early constraints on the L'Aquila earthquake in 2009 estimated a relaxation time of ~1 month (Devoti et al., 2012). Thus, it is very unlikely that we would be observing postseismic uplift for more than one Apennine fault system simultaneously, or that the overall uplift pattern we observe is attributable to transient earthquake cycle deformation.

5.4. Long-Term Uplift?

The arguments above suggest that the uplift features we detect in the GPS data are not attributable to transient processes we have considered, or even ones we have not considered if they operate over the duration of GPS observation. The uplift signal may therefore represent a motion that persists for longer periods of time, possibly over an interval that is geologically relevant. This is supported by the comparison between the geodetically measured uplift and the elevation of uplifted shorelines (Figure 4), and the contours of elevation of Neogene sediments (Figure 5). While comparisons of this nature depend on GPS reference frame realization, alignment, sea level changes, and correction for GIA described in Section 2.2.3, the agreement suggests that the GPS uplift field may be related to formation of the topography of the Apennines. The correlation between the uplift and the active crustal extension further suggests that we are seeing a part of the main geodynamic signal controlling active deformation at the scale of the plate boundary.

6. Discussion

6.1. Vertical Mantle Flow Under the Apennines

Previous work has concluded that support for the residual long wavelength topographic bulge across the Apennines from the mantle (D'Agostino and McKenzie, 1999) helps control the locus of extension generating short wavelength topography (D'Agostino et al., 2001b; D'Agostino et al., 2014; Cowie et al., 2017), and that active continuing uplift measured with geodesy is related to that support (Faccenna et al., 2014b). These indicate that the process (or processes) which generate support continue to the present day, and suggest that mantle does not merely statically support topography, and continues to move upward in a flow that increases support over time. However, it is less clear to what extent surface geodetic observations directly reflect vertical flow of the asthenosphere. We explore this question in the next section by asking: How fast is the vertical flow of the mantle beneath the lithosphere that drives the surface upward?

If the lithosphere is a static plate being displaced upward from its base we might expect the surface to move upward at the same rate. However, the Apennines do not merely rise, they also deform under approximately uniaxial extension as we have seen in our GPS results (Figure 8). When the lithosphere experiences horizontal dilatational strain it is expected to thin and subside (McKenzie, 1978), yet we observe uplift (Figure 3). Thus, the bottom of the lithosphere must be moving upward more rapidly than the observed surface motion to compensate for the stretching-related thinning. We estimate the vertical rate at the bottom of the lithosphere by adding the surface uplift rate expected from the horizontal stretching. We use a relationship based on a model of isostatic compensation of a stretching lithosphere/crust system (McKenzie, 1978) subject to heat flow, but no elastic thickness, that can support a long-term load (from Howell et al, 2017):

$$\dot{S}_i \approx \frac{t_l[(\rho_0-\rho_c)\frac{t_c}{t_l}(1-\alpha T_1\frac{t_c}{2t_l})-\frac{\alpha T_1\rho_0}{2}]}{\rho_0(1-\alpha T_1)-\rho_w}(\dot{e}_1+\dot{e}_2) \qquad (2)$$

$$\dot{S}_i \approx f_i(\dot{e}_1 + \dot{e}_2) \quad (3)$$

Here $\dot{S}_i$ is the surface subsidence rate (positive downward), $\dot{e}_1 + \dot{e}_2$ is the surface horizontal dilatational strain rate. We assume that densities at 0°C for mantle ρ_0 and crust ρ_c to be 3300 and 2700 kg m^{-3} respectively and for water ρ_w to be 1000 kg m^{-3}. The factor f_i in equation (3) is a term containing the physical parameters in equation (2) and scales the dilatational strain rate to estimate the subsidence rate. Following McKenzie et al., (2005) we adopt thermal expansivity $\alpha=3\times10^{-5}$ K^{-1} and test three different values for temperature of the asthenosphere $T_1 = 1215^{\circ}$, 1315°, and 1415° C. We then calculate f_i for an array of possible lithosphere t_l and crustal t_c thicknesses and plot contours of f_i (Figure 11). This shows that the sensitivity of f_i to temperature and lithospheric thickness is relatively small, while sensitivity to crustal thickness is larger.

Since f_i is less sensitive to t_l than to t_c, we fix t_l = 55 km, and test thicknesses for the crust of t_c = 35, 45 or 55 km. Crustal thickness estimated from teleseismic receiver functions is 40-45 km (Piana Agostinetti & Amato, 2009), so we test the others as approximate lower and upper bounds. These parameters result in f_i values of 7900, 10600, and 13300 respectively. These values do not consider thickness of an elastic lithosphere that might reduce the deflection associated with extension, and so are upper bounds. This analysis also ignores the possible contribution of magmatic additions to the lithosphere upon stretching and decompression melting from ascending mantle rocks. As discussed above, Italy has volcanic activity, but is not a volcanically dominated landscape like, e.g., a mid-ocean ridge environment, so we ignore this possible contribution. Also, this model does not account for short wavelength vertical rate variations that may be expected to occur across locked normal fault systems in their interseismic strain accumulation phase, and should only be compared to the long wavelength vertical rate patterns (i.e., gray bands in Figure 4).

We illustrate the effect from stretching on the vertical rate field in the profiles of velocity with the estimated contribution subtracted from the vertical rate field (Figure 12). The profiles of predicted subsidence (where positive subsidence has a negative vertical rate) are shown with the smoothed envelopes of GPS measured uplift (from Figure 4). The dashed lines represent the GPS uplift and the gray band indicates the range of possible upward vertical rates (corrected for extensional-related subsidence). It can also be considered as the vertical component of mantle flow beneath the lithosphere given the assumption outlined above. The width of the gray band is wider since the maximum and minimum addition from the stretching model is added to the upper and lower bound uplift profiles respectively, to reflect the total range of possibilities. The enhancement is greatest where the extensional strain rates are highest.

The vertical motion profiles shown in Figure 12 have fastest rates near the Apennine crest. The northern profile, which prior to enhancement had higher observed uplift west of the crest (near the volcanic fields west of the Apennines) now has similar uplift near the topographic crest of ~1 mm/yr. Relief generation across the profile is 1.5 - 2.0 mm/yr. The central profile has uplift over twice the rate it had prior to enhancement, reaching 0.6 mm/yr, whereas relief generation is 1.0 - 1.5 mm/yr. The southern profile maximum uplift rate exceeds 1 mm/yr, with relieve generation of 1.5 - 1.8 mm/yr. The higher amount of enhancement on the west end of the southern profile comes from strain associated with Campi Flegrei volcanic system which bleeds into the profile area from the north and is not expected to represent subsidence from plate boundary crustal stretching. Owing to its derivation from crustal strain, the vertical rate of upward mantle flow has a greater degree of alignment between plate boundary strain rate and uplift signals.

While it is currently not possible to directly observe the vertical motion of the bottom of the lithosphere with geodetic means, the estimates shown in Figure 12 may serve as a proxy for that motion. These results may be of use to those who model chemical and physical evolution of petrological systems or melt genesis during the ascent of mantle rocks.

6.2. Scale of mantle flow, subducting slab and slab windows

Previous work has suggested that a slab remnant from the period of Neogene Adriatic subduction is sinking in the upper mantle beneath the Apennines. Evidence for this slab exists in seismic imaging (e.g., Giacomuzzi et al., 2011; Piromallo and Morelli, 2003; Spakman et al., 1993; Zhu et al., 2012, and see Faccenna et al. 2014a for a comparison between models). This slab and its lateral segmentation may play a role in driving vertical mantle flow and to have played a role in coordinating surface tectonics and dynamic elevation and uplift (Bennett et al., 2012; Faccenna et al., 2014b; Shaw and Pysklywec, 2007; Wortel and Spakman, 2000). Geodynamic models suggest that the sign of vertical motion expected from a descending high-density slab depends on several factors including e.g., the degree of detachment and rollback of the slab from the overriding lithosphere, viscosity and density structure (Giunchi et al., 1996). Based on early GPS measurement of uplift that seemed to be limited to the central Apennines, and seismic tomography that showed discontinuous high seismic wave speed anomalies in the uppermost mantle, Faccenna et al., (2014b) concluded that the slab was partially detached, which drove uplift to occur in a limited section of the Apennines.

Seismic tomographic models that image wave speed anomalies have limited resolution in Italy. Models show differing degrees of continuity of high waves speed anomalies, which can appear continuous or discontinuous in the mantle beneath the trend of the Apennines, depending on the model and depth range considered. In any case, based on these images it is difficult to confirm the degree of completeness of the dynamic connection between the sinking slab and the upper plate from these images. In at least one model the high wave speed anomaly follows closely our imaged uplift zone, even extending south through the Calabrian Arc into the mantle beneath Sicily (Giacomuzzi et al*.,* 2011). However, even in this model the anomalies are discontinuous at 70 km depth, but continuous at 140 km depth.

In our geodetic imaging of surface motion we observe uplift along the entire length of the Apennine chain, which in light of the arguments presented above would suggest that detachment of the slab from the upper plate is complete. If this is the case it suggests that replacement of high-density sinking slab material with low density asthenospheric mantle is ongoing and its affects are seen by the GPS networks in Italy. It also suggests that because the uplift follows the boundary between Adriatic and Tyrrhenian lithosphere very closely, that uplift, strain, Adriatic microplate translation, and upper mantle flow are all part of a single active and ongoing process that drives contemporary seismic hazard of the Italian Peninsula.

6.3. Flexural Uplift?

Buoyancy of mantle rocks may not be the only possible source of stresses available to drive upward movement of the lithosphere beneath the Apennines. Another possible source is elastic stresses in the extensional axis flanks that drive uplift when thinning of the extending crust unloads the plate. This process, known as of footwall unloading or ridge-flank uplift, results in rift shoulders and tilting that can be evident in topographic or structural profiles parallel to the extension direction. The model has been used to explain observations in the East African Rift (Vening Meinesz, 1950), Rhine Graben (Weissel and Karner, 1989), Sierra Nevada Mountains (Thompson and Parsons, 2010); Baja California (Mueller et al., 2009), Transantarctic Mountains in Antarctica (Stern and Ten Brink, 1989), and others. This model is important to consider because it explains uplift as a process driven primarily by extension, and does not require vertical flow of material in the asthenosphere. Similar to Baja, California, the Apennines have uplifted shorelines far from the axis of uplift (D'Agostino et al., 2001b; Mueller et al., 2009). However, previous analysis of the admittance between gravity and topography has found that the effective elastic thickness of Italy is thin, roughly 3-4 km (D'Agostino and McKenzie, 1999). Thus, the expected horizontal wavelength and curvature of the response to flexure in the Apennines will be narrower than the wide arc of uplift observed in the topography and our geodetic uplift rates (which is between 100 - 150 km in width). Moreover, the Apennines do not exhibit substantially thinner lithosphere that is ostensibly required for unloading of the flanks. These arguments together suggest that it is unlikely that thinning-related unloading alone can explain the observed uplift signal.

However, plate flexure may arise from a source unrelated to thinning and unloading. If asthenospheric flow generates uplift by applying pressure to the base of the plate, then flexure would be a response to the plate bending with the variation in uplift rate across the axis. In this case the flexural stress pattern will be a function of the curvature of the uplift profile and the flexural rigidity, a property related to the thickness of the plate and its elastic properties (Turcotte and Schubert, 2002). If we assume that lithospheric properties are constant we can relate the rate of curving, i.e., the second derivative of uplift rate with respect to distance across axis in the envelopes of uplift (Figure 12), to the rate of flexural bending. In Figure 13 we show the mean of the lower and upper envelopes of filtered uplift rate curvature, calculated from the second derivative of the upper and lower edges of the uplift envelope using double finite difference. In this smoothed version of the curvature we see a pattern, consistent across the north, central and southern profiles, where the greatest rate of flexural bending is not on the flanks but centered on the highest topography and drainage divide of the Apennines. Thus, while the Apennine lithosphere is already under extension from plate boundary divergence (Figure 8), it is also at a local maximum of the flexural extension imparted by uplift that varies across the Apennines. This effect may serve to further focus extension at the locus of maximum uplift.

Multiple mechanisms may be at work to drive the active Apennine uplift, and more detailed mechanical modeling of these effects are likely needed to quantify the relative importance of each contribution. However, the alignment of the separate indicators of crustal deformation, uplift, topography and drainage together suggest that vertical flow-driven flexure can plausibly contribute to the focusing of active seismicity and seismic hazard along the Apennine chain.

7. Conclusions

We have presented a new compilation and analysis of GPS data for Italy and its surrounding areas, and we use GPS Imaging technique to show that the relief of the Apennines Mountain chain in Italy is currently increasing along its entire length by 1 to 2 mm/yr. Relief is increasing in a 100-150 km wide zone with a profile similar to the long wavelength topography, but not similar to the shorter wavelength topography generated by active faulting and erosion. The maximum uplift rates are geographically aligned with the highest elevations, the topographic drainage divide, the location of the highest strain rates associated with extension in the Adriatic/Tyrrhenian plate boundary, and with the areas with fastest uplift rate curvature.

Tests of the variability of the GPS-measured uplift rate, GRACE satellite mission data, and correlation of the uplift with other data pertaining to long-term uplift suggest that it is a long-lived feature.

Uplift occurs despite that the expected consequence of extension is crustal thinning and subsidence. This is consistent with the presence of asthenospheric upward mantle flow of up to 2 mm/yr, possibly associated with buoyant mantle flowing into the space above a sinking slab that is dynamically detached from the upper plate.

These results also suggest that the gravitational forces responsible for the correlation between regional high elevation and active extension in the Apennines, have been excited in the last 2-3 My by the same process that is imaged by the dense GPS network in the Apennines. Spatial scales and amplitudes of vertical motion geodetically observed in the Apennines are consistent with multiscale mantle convection processes inducing dynamic topography at a wide range of scales (Arnould et al., 2018; Hoggard et al., 2016; Kreemer et al., 2020). Continental scale GPS imaging of vertical land motion can provide additional constraints available for studies targeting the topographic expression of mantle flow.

Acknowledgements

We thank the operators and data archiving facilities of the 26 high-precision GPS networks in and around Italy that we used for this study, the internet locations from which data were accessed are listed individually in Supplemental Table 1. We obtained GRACE time series data via the University of Colorado Mascon Visualization Tool (https://ccar.colorado.edu/grace/index.html). WCH received support from NASA Solid Earth via projects NSSC17K0565, NNH16ZDA001N, and 80NSSC19K1044 from the University of Nevada, Reno for his sabbatical leave and for travel support via the International Activities grant program. Some figures were made using the Generic Mapping Tools v5.4.1 software (Wessel et al., 2013). WCH acknowledges support from INGV who hosted his visit in Rome.

References

Albano, M., Barba, S., Saroli, M., Moro, M., Malvarosa, F., Costantini, M., Bignami, C., & Stramondo, S. (2015). Gravity-driven postseismic deformation following the Mw 6.3 2009 L'Aquila (Italy) earthquake. *Scientific Reports, 5*, 16558, https://doi.org/10.1038/srep16558.

Altamimi, Z., Rebischung, P., Métivier, L., & Collilieux, X. (2016). ITRF2014: A new release of the International Terrestrial Reference Frame modeling nonlinear station motions. *J. Geophys. Res. - Solid Earth,* 121, 6109-6131, https://doi.org/10.1002/2016JB013098.

Amos, C. B., Audet, P., Hammond, W. C., Bürgmann, R., Johanson, I. A., & Blewitt, G. (2014). Uplift and seismicity driven by groundwater depletion in central California. *Nature*, *509*(7501), 483–486. https://doi.org/10.1038/nature13275.

Argus, D. F., Fu, Y., & Landerer, F. W. (2014). Seasonal variation in total water storage in California inferred from GPS observations of vertical land motion. *Geophys. Res. Lett., 41*, 1971–1980, https://doi.org/10.1002/2014GL059570.

Argus, D. F., Landerer, F. W., Wiese, D. N., Martens, H. R., Fu, Y., Famiglietti, J. S., & Watkins, M. M. (2017). Sustained water loss in California's mountain ranges during severe drought from 2012 to 2015 inferred from GPS. *J. Geophys. Res.- Solid Earth, 122*, 10,559–10,585. https://doi.org/10.1002/ 2017JB014424.

Arnould, M., Coltice, N., Flament, N., Seigneur, V., & Müller, R. D. (2018). On the scales of dynamic topography in whole-mantle convection models. *Geochemistry, Geophysics, Geosystems*, *19(*9) 3140-3163, https://doi.org/10.1029/2018GC007516.

Bartolini, C., D'Agostino, N., & Dramis, F., (2003). Topography, exhumation, and drainage network evolution of the Apennines. *Episodes*, *26*(3), 212-216, https://doi.org/10.18814/epiiugs/2003/v26i3/010.

Batini F., Brogi, A, Lazzarotto A., Liotta, D., & Pandeli, E. (2003). Geological features of Larderello Travale and Mt. Amiata geothermal areas (southern Tuscany, Italy). *Episodes 26(*3*),* p. 239-244, https://doi.org/10.18814/epiiugs/2003/v26i3/015.

Bennett, R. A., Serpelloni, E., Hreinsdóttir, S., Brandon, M. T., Buble, G., Basic, T., Casale, G., Cavaliere, A., Anzidei, M., Marjonovic, M., Minelli, G., Molli, G., & Montanari, A. (2012). Syn-convergent extension observed using the RETREAT GPS network, northern Apennines, Italy. *J. Geophys. Res., 117*, B4, https://doi.org/10.1029/2011JB008744.

Blewitt, G., Kreemer, C., Hammond, W.C., & Gazeaux, J. (2016). MIDAS Robust Trend Estimator for Accurate GPS Station Velocities Without Step Detection. *J. Geophys. Res. - Solid Earth*, 121(30, 2054-2068, https://doi.org/10.1002/2015JB012552.

Blewitt, G., Hammond, W.C., & Kreemer, C. (2018). Harnessing the GPS data explosion for interdisciplinary science, *Eos, 99*, https://doi.org/10.1029/2018EO104623.

Bock, Y., Wdowinski, S., Ferretti, A., Novali, F., & Fumagalli, A. (2012). Recent subsidence of the Venice Lagoon from continuous GPS and interferometric synthetic aperture radar, *Geochem. Geophys. Geosyst., 13*, Q03023, https://doi.org/10.1029/2011GC003976.

Bonaccorso, A., Bonforte, A. & Gambino, S. (2015). Twenty-five years of continuous borehole tilt and vertical displacement data at Mount Etna: Insights on long-term volcanic dynamics. *Geophys. Res. Lett., 42,* 10,222–10,229, https://doi.org/10.1002/2015GL066517.

Carminati, E., Doglioni, C., & Scrocca, D. (2003). Apennines subduction-related subsidence of Venice (Italy). *Geophys. Res. Lett., 30*(13), 1717, https://doi.org/10.1029/2003GL017001.

Cecconi, M., Scarapazzi, M. Viggiani, G.M. B. (2010). On the geology and the geotechnical properties of pyroclastic flow deposits of the Colli Albani. *Bull. Eng. Geol. Env.*, *69*(2): 185–206, https://doi.org/10.1007/s10064-009-0250-x.

Cenni, N., Viti, M., Baldi, P., Mantovani, E., Bacchetti, M., Vannucchi, A., (2013). Present vertical movements in Central and Northern Italy from GPS data: Possible role of natural and anthropogenic causes. *J. Geodynamics, 71* (2013) 74–85, https://doi.org/10.1016/j.jog.2013.07.004.

Cheloni, D., + 12 authors (2014). Coseismic and post-seismic slip of the 2009 L'Aquila (central Italy) M_W 6.3 earthquake and implications for seismic potential along the Campotosto fault from joint inversion of high-precision levelling, InSAR and GPS data. *Tectonophysics 622*, 168–185, https://doi.org/10.1016/j.tecto.2014.03.009.

Cheloni, D., + 41 authors (2017). Geodetic model of the 2016 Central Italy earthquake sequence inferred from InSAR and GPS data. *Geophys. Res. Lett., 44*, 6778–6787, https://doi.org/10.1002/2017GL073580.

Chen, W., Braitenburg, C., & Serpelloni, E. (2018). Interference of tectonic signals in subsurface hydrologic monitoring through gravity and GPS due to mountain building. *Global and Planetary Change, 167*, p 148-159, https://doi.org/10.1016/j.gloplacha.2018.05.003.

Chanard, K., Avouac, J. P., Ramillien, G. & Genrich, J. (2014). Modeling deformation induced by seasonal variations of continental water in the Himalaya region: Sensitivity to Earth elastic structure. *J. Geophys. Res. - Solid Earth, 119,* 5097–5113, https://doi.org/10.1002/2013JB010451.

Cinque, A., Patacca, A., Scandone, P., & Tozzi, M. (1993). Quaternary kinematic evolution of the Southern Apennines, Relationships between surface geological features and deep lithospheric structures. *Ann. Geofis., 36*, 249–260.

Cintorrino A. A., Palano, M., Viccaro, M. (2019). Magmatic and tectonic sources at Vulcano (Aeolian Islands, Southern Italy): A geodetic model based on two decades of GPS observations. *J. Volcan. Geothermal Res., 388,* https://doi.org/10.1016/j.jvolgeores.2019.106689.

Cosentino, D. & Fubelli, G. (2008). Comment on: "Geomorphological, paleontological and $^{87}Sr/^{86}Sr$ isotope analyses on early Pleistocene paleoshorelines to define the uplift of Central Apennines (Italy)." *Quaternary Research, 69*, 163–164, https://doi.org/10.1016/j.yqres.2007.07.014.

Cosentino, D., Asti, R., Nocentini, M., Gliozzi, E., Kotsakis, T., Mattei, M., Esu, D., Spadi, M., Tallini, M., Cifelli, F., & Pennacchioni, M., (2017). New insights into the onset and evolution of the central Apennine extensional intermontane basins based on the tectonically active L'Aquila Basin (central Italy). *Geol. Soc. Am. Bull. 129* (9–10), 1314–1336.

D'Agostino, N. & McKenzie, D. (1999). Convective support of long-wavelength topography in the Apennines (Italy). *Terra Nova, 11*, 234-238, https://doi.org/10.1046/j.1365-3121.1999.00252.x.

D'Agostino, N., Giuliani, R. Mattone, M., & Bonci, L. (2001a). Active crustal extension in the central Apennines (Italy) inferred from GPS measurements in the interval 1994-1999. *Geophys. Res. Lett., 28*, 2121-2124, https://doi.org/10.1029/2000GL012462.

D'Agostino, N., Jackson, J.A., Dramis, F., & Funiciello, F. (2001b). Interactions between mantle upwelling, drainage evolution and active normal faulting: an example from the central Apennines (Italy). *Geophys. J. Int.,* 147, 475–497, https://doi.org/10.1046/j.1365-246X.2001.00539.x.

D’Agostino, N., Avallone, A., Cheloni, D., D’Anastasio, E., Mantenuto, S., & Selvaggi, G. (2008). Active tectonics of the Adriatic region from GPS and earthquake slip vectors, *J. Geophys. Res. - Solid Earth*, *113*, B12413, https://doi.org/10.1029/2008JB005860.

D’Agostino, N., Mantenuto, S., D’Anastasio, E., Giuliani, R., Mattone, M., Calcaterra, S., Gambino, P., & Bonci, L. (2011). Evidence for localized active extension in the central Apennines (Italy) from global positioning system observations. *Geology*, *v. 39*, n. 4, p. 291–294, https://doi.org/10.1130/G31796.1.

D’Agostino, N., Cheloni, D., Fornaro, G., Giuliani, R., & Reale, D. (2012). Space-time distribution of afterslip following the 2009 L’Aquila earthquake. *J. Geophys. Res., 117,* B02402, https://doi.org/10.1029/2011JB008523.

D'Agostino, N., England, P., Hunstad, I., & Selvaggi, G. (2014). Gravitational potential energy and active deformation in the Apennines. *Earth Planet. Sci. Lett., v. 397*, p. 121-132, https://doi.org/10.1016/j.epsl.2014.04.013.

D’Agostino, N., Silverii, F., Amoroso, O., Convertito, V., Fiorillo, F., Ventafridda, G., & Zollo, A. (2018). Crustal deformation and seismicity modulated by groundwater recharge of karst aquifers. *Geophys. Res. Lett, 45* (22), p. 12,253-12,262, https://doi.org/10.1029/2018GL079794.

D’Anastasio, E., De Martini, P. M., Selvaggi, G., Pantosti, D., Marchioni, A., & Maseroli, R. (2006). Short-term vertical velocity field in the Apennines (Italy) revealed by geodetic levelling data. *Tectonophysics, 418*(3–4), 219–234, https://doi.org/10.1016/j.tecto.2006.02.008.

Devoti. R., Esposito, A., Pietrantonio, G., Pisani, A. R., Riguzzi, F. (2011), Evidence of large scale deformation patterns from GPS data in the Italian subduction boundary. *Earth Planet. Sci. Lett., 311*, 230–241, https://doi.org/10.1016/j.epsl.2011.09.034.

Devoti, R., Anderlini, L., Anzidei, M., Esposito, A., Galvani, A., Pietrantonio, G., Pisani A., Riguzzi, F., Sepe, V., & Serpelloni, E. (2012). The coseismic and postseismic deformation of the L’Aquila, 2009 earthquake from repeated GPS measurements. *Ital. J. Geosci. v 131*, n. 3 (2012), 348-358, https://doi.org/10.3301/IJG.2012.15.

Elter, P., Grasso, M., Parotto, M., & Vezzani, L., (2003). Structural setting of the Alpine-Maghrebian thrust belt. *Episodes, v. 26*, n. 3, p. 205–211, https://doi.org/10.18814/epiiugs/2003/v26i3/009.

Faccenna, C., Becker, T. W., Auer, L., Billi, A., Boschi, L., Brun, J.P., Capitanio, F. A., Funiciello, F., Horvàth, F., Jolivet, L., Piromallo, C., Royden, L., Rossetti, F., & Serpelloni, E. (2014a), Mantle dynamics in the Mediterranean. *Rev. Geophys.*, 52(3), 283-332, https://doi.org/10.1002/2013RG000444.

Faccenna, C., Becker, T. W., Miller, M. S., Serpelloni, E., & Willett, S. D. (2014b). Isostasy, dynamic topography, and the elevation of the Apennines of Italy. *Earth Planet. Sci. Lett.*, 407 163–174, https://dx.doi.org/10.1016/j.epsl.2014.09.027.

Freda, C, Gaeta, M., Karner, D.B., Marra, F., Renne, P. R., Taddeucci, J., Scarlato, P., Christensen, J.N, & Dallai, L. (2006). Eruptive history and petrologic evolution of the Albano multiple maar (Alban Hills, Central Italy). *Bull. Volc., 68*: 567–591, https://doi.org/10.1007/s00445-005-0033-6.

Fu, Y., & Freymueller, J. T. (2012). Seasonal and long-term vertical deformation in the Nepal Himalaya constrained by GPS and GRACE measurements. *J. Geophys. Res., 117*, B03407, https://doi.org/10.1029/2011JB008925.

Fu, Y., Argus, D. F. & Landerer, F. W. (2015). GPS as an independent measurement to estimate terrestrial water storage variations in Washington and Oregon. *J. Geophys. Res. - Solid Earth, 120*, 552–566, https://doi.org/10.1002/2014JB011415.

Galli, P., Galadini., F., Pantosti, D., (2008). Twenty years of paleoseismology in Italy, *Earth-Science Reviews, 88*, 89–117. https://doi.org/10.1016/j.earscirev.2008.01.001.

Galandini, F., & Galli, P. (2003). Paleoseismology of silent faults in the Central Apennines (Italy): the Mt. Vettore and Laga Mts. faults. *Annals of Geophysics, 46*,(5). https://doi.org/10.4401/ag-3457.

Gatto, P., & Carbognin, L. (1981). The lagoon of Venice: Natural environmental trend and man-induced modification, *Hydrol. Sci. Bull., 26*(4), 379–391, https://doi.org/10.1080/02626668109490902.

Geurts, A.H., Cowie, P. A., Duclaux, G., Gawthorpe, R. L., Huismans, R. S., Pedersen, V. K., Wedmore, L. N. J. (2018). Drainage integration and sediment dispersal in active continental rifts: A numerical modelling study of the central Italian Apennines, *Basin Research*, *30*(5), 965-989, https://doi.org/10.1111/bre.12289.

Giacomuzzi, G., Chiarabba, C., De Gori, P. (2011). Linking the Alps and Apennines subduction systems: New constraints revealed by high-resolution teleseismic tomography. *Earth Planet. Sci. Lett. 301*, 531–543, https//doi.org/10.1016/j.epsl.2010.11.033.

Gianelli, G., Manzella, A., & Puxeddu, M. (1997). Crustal models of the geothermal areas of southern Tuscany (Italy). *Tectonophysics, v. 281*, 3-4, p. 221-239, https://doi.org/10.1016/S0040-1951(97)00101-7.

Giunchi, C., Sabadini, R., Boschi, E., & Gasperini, P. (1996). Dynamic models of subduction: geophysical and geological evidence in the Tyrrhenian Sea. *Geophys. J. Int.,* 126, p. 555-578, https://doi.org/10.1111/j.1365-246X.1996.tb05310.x.

Gourmelen, N. & Amelung, F., (2005). Postseismic Mantle Relaxation in the Central Nevada Seismic Belt. *Science, 310*, 1473-1476. https://doi.org/10.1126/science.1119798.

Hammond, W.C., Blewitt, G. & Kreemer, C. (2016). GPS Imaging of vertical land motion in California and Nevada: Implications for Sierra Nevada uplift. *J. Geophys. Res. - Solid Earth*, 121, 10, 7681-7703, https://doi.org/10.1002/2016JB013458.

Hammond, W. C., Kreemer, C., Zaliapin, I., & Blewitt, G. (2019). Drought-triggered magmatic inflation, crustal strain, and seismicity near the Long Valley Caldera, Central Walker Lane. *J. Geophys. Res.- Solid Earth, 124*, https://doi.org/ 10.1029/2019JB017354.

Haskell, N.A., (1935). The motion of a viscous fluid under a surface-load with particular reference to the Pleistocene ice-sheets, *Eos, 16*(1), p.104, https://doi.org/10.1029/TR016i001p00104-1.

Hoggard, M., White, N., Al-Attar, D (2016). Global dynamic topography observations reveal limited influence of large-scale mantle flow. *Nature Geosci.*, *9*, 456–463, https://doi.org/10.1038/ngeo2709.

Howell, A., Jackson, J., Copley, A. A., McKenzie, D., & Nissen, E. (2017). Subduction and vertical coastal motions in the eastern Mediterranean. *Geophys. J. Int., 211*, 593–620, https://doi.org/10.1093/gji/ggx307.

Isaia, R., Marianelli, P., & Sbrana, A., (2009). Caldera unrest prior to intense volcanism in Campi Flegrei (Italy) at 4.0 ka B.P.: Implications for caldera dynamics and future eruptive scenarios. *Geophys. Res. Lett., 36*(21)*,* L21303, https://doi.org/10.1029/2009GL040513.

Kligfield, R., (1979). The Northern Apennines as a collisional orogen. *J. Sci., 279*, 676-691, https://doi.org/10.2475/ajs.279.6.676.

Kreemer, C., Blewitt, G. & Klein, E. C. (2014), A geodetic plate motion and Global Strain Rate Model, *Geochem. Geophys. Geosyst., 15*, 3849–3889, https://doi.org/10.1002/2014GC005407.

Kreemer, C., Blewitt, G. & Davis, P.M. (2020). Geodetic evidence for a buoyant mantle plume beneath the Eifel volcanic area. NW Europe, EarthArXiv, https://eartharxiv.org/yab5d/.

Lambeck, K., Smither, C. & Johnston, P. (1998). Sea-level change, glacial rebound and mantle viscosity for northern Europe. *Geophys. J. Int., 134*, 102–144, https://doi.org/10.1046/j.1365-246x.1998.00541.x

Luthcke, S.B., Sabaka, T.J. Loomis, B.D., Arendt, A.A., McCarthy, J.J. & Camp, J. (2013). Antarctica, Greenland and Gulf of Alaska land ice evolution from an iterated GRACE global mascon solution. *J. Glac. 59*(216), 613-631, https://doi.org/10.3189/2013JoG12J147.

Malinverno, A. & Ryan, W.B.F. (1986). Extension in the Tyrrhenian Sea and shortening in the Apennines as result of arc migration driven by sinking of the lithosphere. *Tectonics*, *v. 5*, n. 2, p 227-245, https://doi.org/10.1029/TC005i002p00227.

Mancini, M., D'Anastasio, E., Barbieri, M., & De Martini, P. M. (2007). Geomorphological, paleontological and $^{87}Sr/^{86}Sr$ isotope analyses of early Pleistocene paleoshorelines to define the uplift of Central Apennines (Italy). *Quaternary Res. 67*, p. 487–501, https://doi.org/10.1016/j.yqres.2007.01.005.

Marinelli, G., Barberi, F., & Cioni, R. (1993). Sollevamenti neogenici e intrusioni acide della Toscana e del Lazio settentrionale. *Mem. Soc. Geol. It., 49*, 279–288.

Martini, I.P., & Sagri, M. (1993). Tectono-sedimentary characteristics of Late Miocene-Quaternary extensional basins of the Northern Apennines, Italy. *Earth-Science Reviews, 34*(3), 197-233, ISSN 0012-8252, https://doi.org/10.1016/0012-8252(93)90034-5.

McKenzie, D., (1978). Some remarks on the development of sedimentary basins. *Earth planet. Sci. Lett., 40*(1), 25–32, https://doi.org/10.1016/0012-821X(78)90071-7.

McKenzie, D., Jackson, J., & Priestley, K., (2005). Thermal structure of oceanic and continental lithosphere. *Earth planet. Sci. Lett.,* 233(3), 337– 349, https://doi.org/10.1016/j.epsl.2005.02.005.

Mueller, K., Kier, G., Rockwell, T. & Jones, C. H. (2009). Quaternary rift flank uplift of the Peninsular Ranges in Baja and southern California by removal of mantle lithosphere. *Tectonics, 28,* TC5003, https://doi.org/10.1029/2007TC002227.

Oldow, J. S., Ferranti, L., Lewis, D. S., Campbell, J. K., D'Argenio, B., Catalano, R., Pappone, G., Carmignani, L., Conti, P., & Aiken, C. L. V. (2002). Active fragmentation of Adria, the north African promontory, central Mediterranean. *Geology, v. 30*, n. 9, p. 779-782, https://doi.org/10.1130/0091-7613(2002)030<0779:AFOATN>2.0.CO;2.

Ori, G. G., Serafini, G., Visentini, G., Lucchi, F. R., Casnedi, R., Colalongo, M. L. & Mosna, S., (1993). Depositional history of the Pliocene-Pleistocene Adriatic foredeep (Central Italy) from surface and subsurface data, *in Generation, Accumulation and Production of Europe's Hydrocarbon III,* pp. 233–258, ed. Specer, A.M., Spec. Publ., Eur. Ass. Petr. Geosc., 3.

Pace, P., Scisciani, V., Calamita, F., Butler, R. W. H., Iacopini, D., Esestime, P., Hodgson, N., (2015). Inversion structures in a foreland domain: Seismic examples from the Italian Adriatic Sea. *Interpretation,* https://dx.doi.org/10.1190/INT-2015-0013.1

Patacca, E., & Scandone, P., (1989). Post-Tortonian mountain building in the Apennines. The role of the passive sinking of a relic lithospheric slab, *in* Boriani, A., Bonafede, M., Piccardo, G.B., and Vai, G.B., eds., *The Lithosphere in Italy: Atti dei Convegni Lincei, v. 80*, p. 157–176.

Peltier, W. R. (2004). Global glacial isostasy and the surface of the ice-age Earth: The ICE-5G (VM2) model and GRACE. *Annu. Rev. Earth Planet. Sci., 32*(1), 111–149, https://doi.org/10.1146/annurev.earth.32.082503.144359.

Peltier, W. R., Argus, D. F. & Drummond, R. (2015). Space geodesy constrains ice age terminal deglaciation: The global ICE-6G_C (VM5a) model. *J. Geophys. Res. - Solid Earth*, 120, 450–487, https://doi.org/10.1002/2014JB011176.

Piana Agostinetti, N., & Amato, A. (2009). Moho depth and V_p/V_s ratio in peninsular Italy from teleseismic receiver functions. *J. Geophys. Res., 114,* B06303, https://doi.org/10.1029/2008JB005899.

Piromallo, C., & Morelli, A. (2003). *P* wave tomography of the mantle under the Alpine-Mediterranean area. *J. Geophys. Res., 108(*B2), 2065, https://doi.org/10.1029/2002JB001757.

Pizzi, A. (2003). Plio-Quaternary uplift rates in the outer zone of the central Apennines fold-and-thrust belt, Italy. *Quaternary International, v. 101–102*, p. 229-237, https://doi.org/10.1016/S1040-6182(02)00105-2.

Rebischung, P., Altamimi, Z., Ray, J., & Garayt, B. (2016). The IGS contribution to ITRF2014. *J. Geod., 90,* 7, 611–630, https://doi.org/10.1007/s00190-016-0897-6.

Reilinger, R. (1986). Evidence for postseismic viscoelastic relaxation following the 1959 M- 7.5 Hebgen Lake, Montana, earthquake. *J. Geophys. Res, v. 91*(B9), 9488-9494, https://doi.org/10.1029/JB091iB09p09488.

Riguzzi, F., Crespi, M., Devoti, R., Doglioni, C., Pietrantonio, G. Pisani A.R. (2013). Strain rate relaxation of normal fault and thrust faults in Italy. *Geophys. J. Int.*, https://doi.org/10.1093/gji/ggt304.

Rovida A., Locati M., Camassi R., Lolli B., Gasperini P. (eds), 2019. Italian Parametric Earthquake Catalogue (CPTI15), version 2.0. Istituto Nazionale di Geofisica e Vulcanologia (INGV). https://doi.org/10.13127/CPTI/CPTI15.2.

Royden, L., Patacca, E., & Scandone, P. (1987). Segmentation and configuration of subducted lithosphere in Italy: An important control on thrust-belt and foredeep-basin evolution. *Geology, 15,* 714-717, https://doi.org/10.1130/0091-7613(1987)15<714:SACOSL>2.0.CO;2.

Savage, J. C., Gan, W., & Svarc, J. L. (2001). Strain accumulation and rotation in the Eastern California Shear Zone. *J. Geophys. Res. - Solid Earth*, *106*(B10), 21,995–22,007, https://doi.org/10.1029/2000JB000127.

Sen, P. K. (1968). Estimates of the regression coefficient based on Kendall’s tau. *J. Am. Stat. Assoc., 63,* 1379–1389.

Serpelloni, E., Anzidei, M., Baldi, P., Casula G., & Galvani, A. (2005). Crustal velocity and strain-rate fields in Italy and surrounding regions: new results from the analysis of permanent and non-permanent GPS networks. *Geophys. J. Int., 161*, 861–880, https://doi.org/10.1111/j.1365-246X.2005.02618.x.

Serpelloni, E., Faccenna, C., Spada, G., Dong, D. & Williams, S. D. P. (2013). Vertical GPS ground motion rates in the Euro-Mediterranean region: New evidence of velocity gradients at different spatial scales along the Nubia-Eurasia plate boundary. *J. Geophys. Res., 118,* https://doi.org/10.1002/2013JB010102.

Serri, G., Innocenti, F., & Mentti, P., (1993). Geochemical and petrological evidence of the subduction of delaminated Adriatic continental lithosphere in the genesis of the Neogene-Quaternary magmatism of central Italy, *Tectonophysics*, *223*(1), 117-147, https://doi.org/10.1016/0040-1951(93)90161-C.

Shaw, M., & Pysklywec, R. (2007). Anomalous uplift of the Apennines and subsidence of the Adriatic: The result of active mantle flow? *Geophys. Res. Lett., 34*, L04311, https://doi.org/10.1029/2006GL028337.

Silverii, F., D'Agostino, N., Métois, M., Fiorillo, F., & Ventafridda, G. (2016). Transient deformation of karst aquifers due to seasonal and multiyear groundwater variations observed by GPS in southern Apennines (Italy). *J. Geophys. Res. - Solid Earth*, *121*, 8315–8337 https://doi.org/10.1002/2016JB013361.

Spakman, W., van der Lee, S., & van der Hilst, R. (1993). Travel-time tomography of the European-Mediterranean mantle down to 1400 km. *Phys. Earth Planet. Inter., 79*, 3–74.

Stern, T. A., & Ten Brink, U. S. (1989). Flexural uplift of the Transantarctic Mountains. *J. Geophys. Res., 94,* 10,315–10,330, doi:10.1029/JB094iB08p10315.

Stucchi, M., Meletti, C., Montaldo, V., Crowley, H., Calvi, G. M., & Boschi, E. (2011). Seismic hazard assessment (2003–2009) for the Italian building code. *Bull. Seismol. Soc. Am.*, *101*, 1885–1911, https://doi.org/10.1785/0120100130.

Theil, H. (1950). A rank-invariant method of linear and polynomial regression analysis. *Indag. Math., 12,* 85–91.

Thompson, G. A. & Parsons, T. (2009). Can footwall unloading explain late Cenozoic uplift of the Sierra Nevada crest? *Int. Geol. Rev., 51,* 9, 986-993, https://doi.org/10.1080/00206810903059156.

Tosi, L., Carbognin, L., Teantini, P., Strozzi, T., & Wegmüller, U. (2002), Evidence of the present relative land stability of Venice, Italy, from land, sea, and space observations. *Geophys. Res. Lett., 29*(12), 1562, https://doi.org/10.1029/2001GL013211.

Turcotte, D.L., & Schubert, G. (2002). Geodynamics, 2nd Edition, Cambridge University Press.

Vening Meinesz, F.A., (1937). The determination of the Earth's plasticity from the postglacial uplift of Scandinavia: isostatic adjustment. *Kon. Akad. Wettensch, 40*, 654–662.

Vening Meinesz, F. A. (1950). Les graben africains, résultat de compression ou de tension dans la croûte terrestre? *Inst. R. Colon. Belge Bull., 21*, 539 – 552.

Watkins, M. M., Wiese, D. N., Yuan, D.-N. Boening, C. & Landerer, F. W. (2015). Improved methods for observing Earth's time variable mass distribution with GRACE using spherical cap mascons. *J. Geophys. Res. - Solid Earth, 120*(4), 2648-2671, https://doi.org/10.1002/2014JB011547.

Wdowinski, S., Bock, Y., Zhang, J., Fang, P., Genrich, J., (1997). Southern California Permanent GPS Geodetic Array: Spatial filtering of daily positions for estimating coseismic and postseismic displacements induced by the 1992 Landers earthquake, *J. Geophys. Res. - Solid Earth, 102*(B8), 18,057-18070, https://doi.org/10.1029/97JB01378.

Weissel, J. K., & Karner, G. D. (1989). Flexural uplift of rift flanks due to mechanical unloading of the lithosphere during extension. *J. Geophys. Res., 94,* 13,919 – 13,950, https://doi.org/10.1029/JB094iB10p13919.

Wessel, P., Smith, W. H. F., Scharroo, R., Luis, J. F., & Wobbe, F. (2013). Generic Mapping Tools: Improved version released. *Eos, Trans. Am. Geophys. Union, 94(45*), 409–410. https://doi.or g/10.1002/2013EO450001.

Wiese, D. N., Landerer, F. W. & Watkins, M. M. (2016). Quantifying and reducing leakage errors in the JPL RL05M GRACE mascon solution. *Water Resour. Res., 52*, 7490–7502, https://doi.org/10.1002/2016WR019344.

Wortel, M.J.R., & Spakman, W. (2000). Subduction and slab detachment in the Mediterranean-Carpathian region. *Science, v. 290*, p. 1910-1917, https://doi.org/10.1126/science.290.5498.1910.
Zhu, H., Bozdag, E., Peter, D., & Tromp, J. (2012). Structure of the European upper mantle revealed by adjoint tomography. *Nat. Geosci., 5*, 493–498, https://doi.org/10.1038/ngeo1501

Figures and Captions

Figure 1

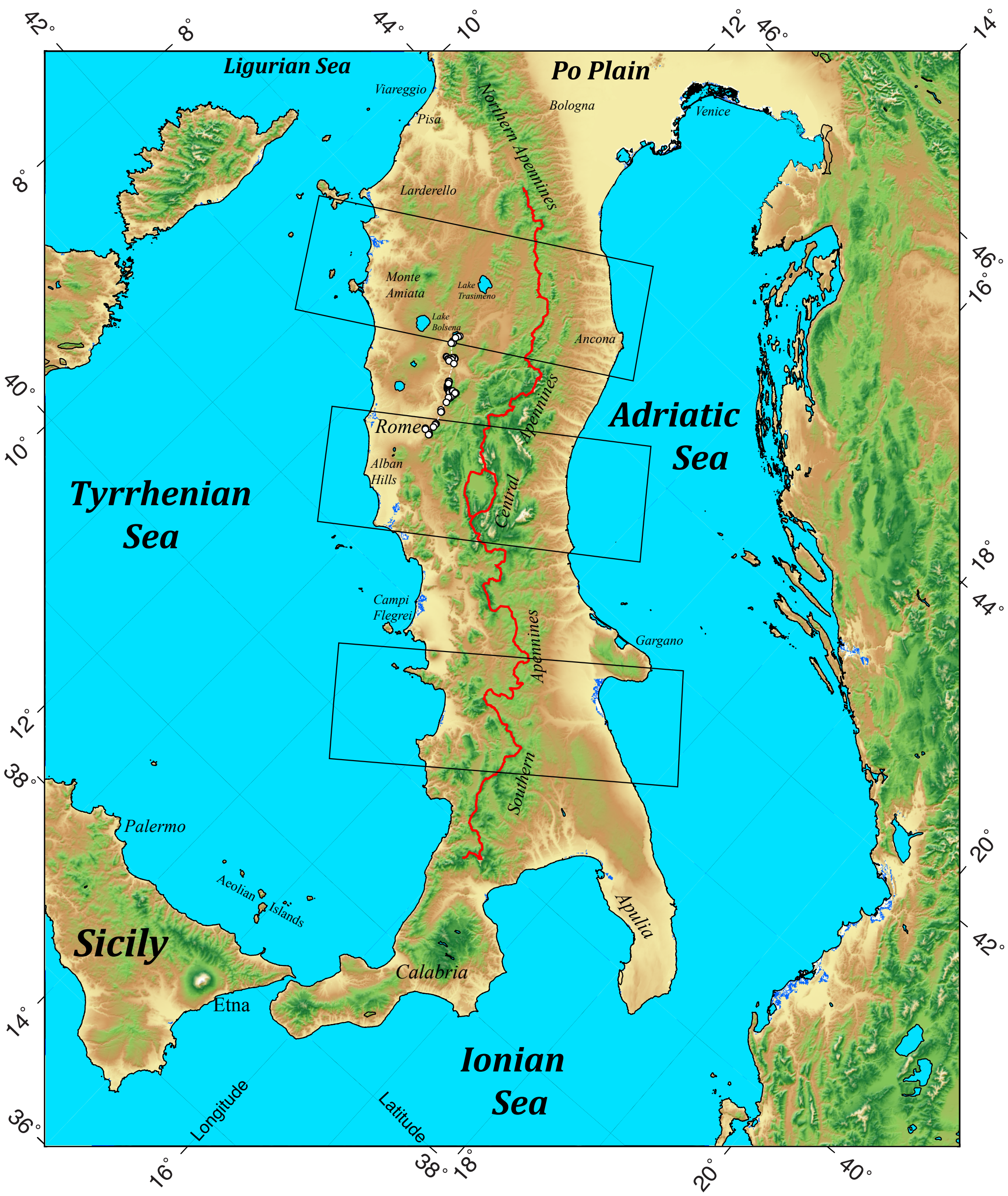

Figure 1. Color shaded topography of Apennines, Italy and nearby locations. Red line indicates location of topographic drainage divide along the crest of the Apennines. Black rectangles indicate location of three profiles extending from Tyrrhenian to Adriatic seas used in later figures. White circles with black outline connected by white dashed line depict the location of observed Pleistocene shoreline of Mancini et al., (2007).

Figure 2.

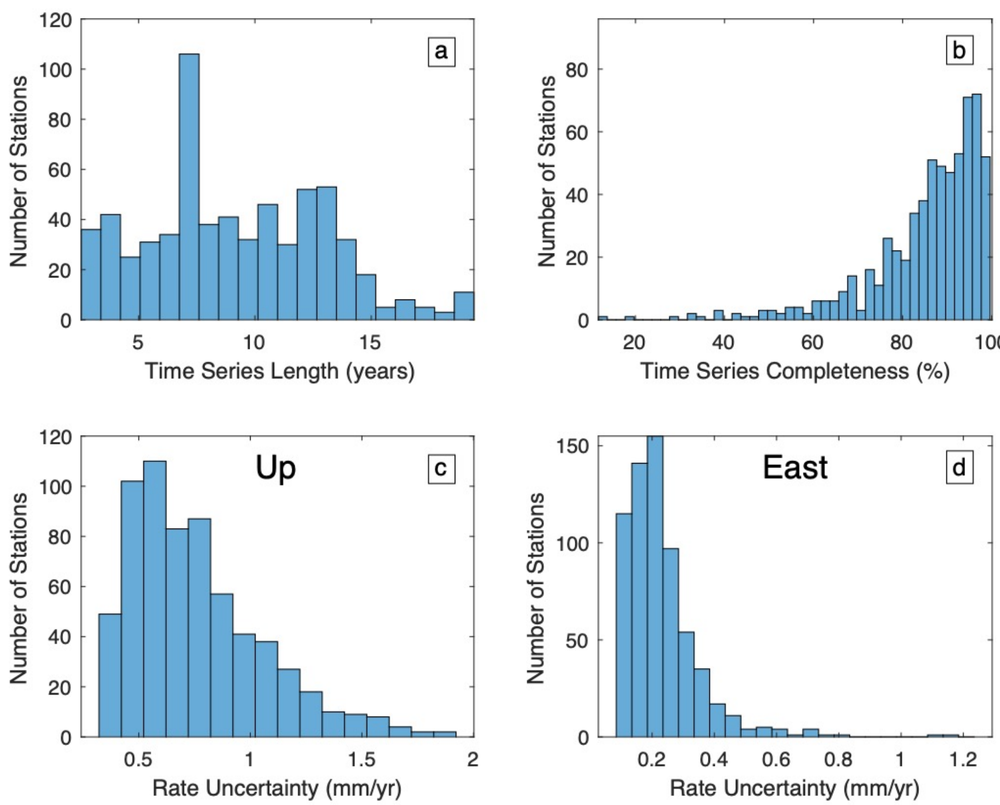

Figure 2. Statistics of time series that are used in the GPS Imaging. a) Histogram of time series duration in years. b) Histogram of completeness of time series, where 100% indicates there are no data gaps between first and last observation. c) Histogram of the uncertainty of the MIDAS rates from the vertical time series. d) Histogram of the uncertainty of the MIDAS east rate, which is similar to that or the north rate (but is not shown).

Figure 3.

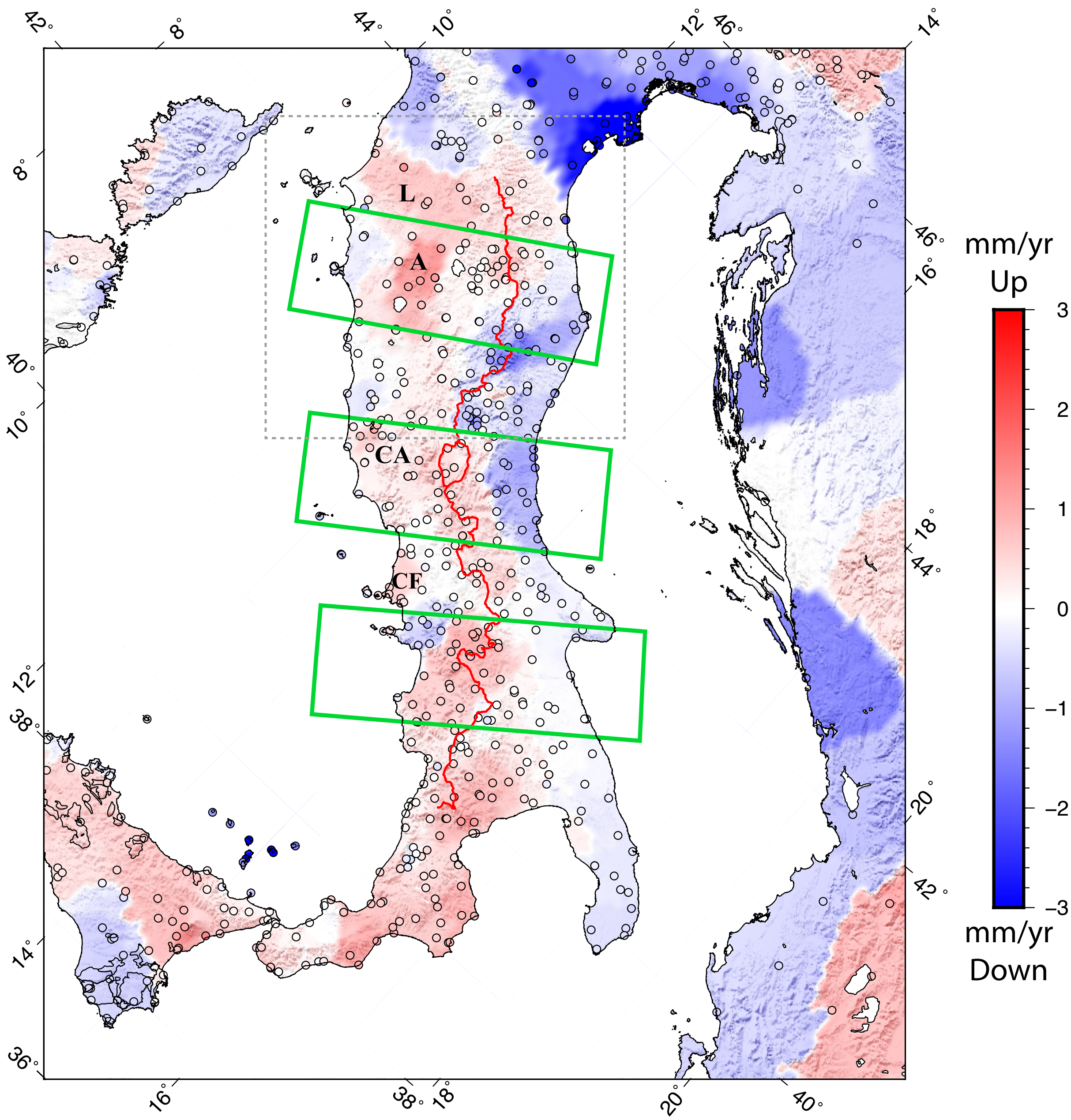

Figure 3. Result of GPS Imaging of vertical rate for Italy and surrounding regions, corrected for the effects of GIA. Color scale is in mm/yr, red upward, blue downward. Circles indicate location of GPS stations. Color of each station circle indicates the median filtered vertical rate value for the station. Green rectangles indicate location of velocity profiles. Labels indicate locations discussed in text, L, Larderello; A, Amiata; CA, Colli Albani; CF, Campi Flegrei.

Figure 4.

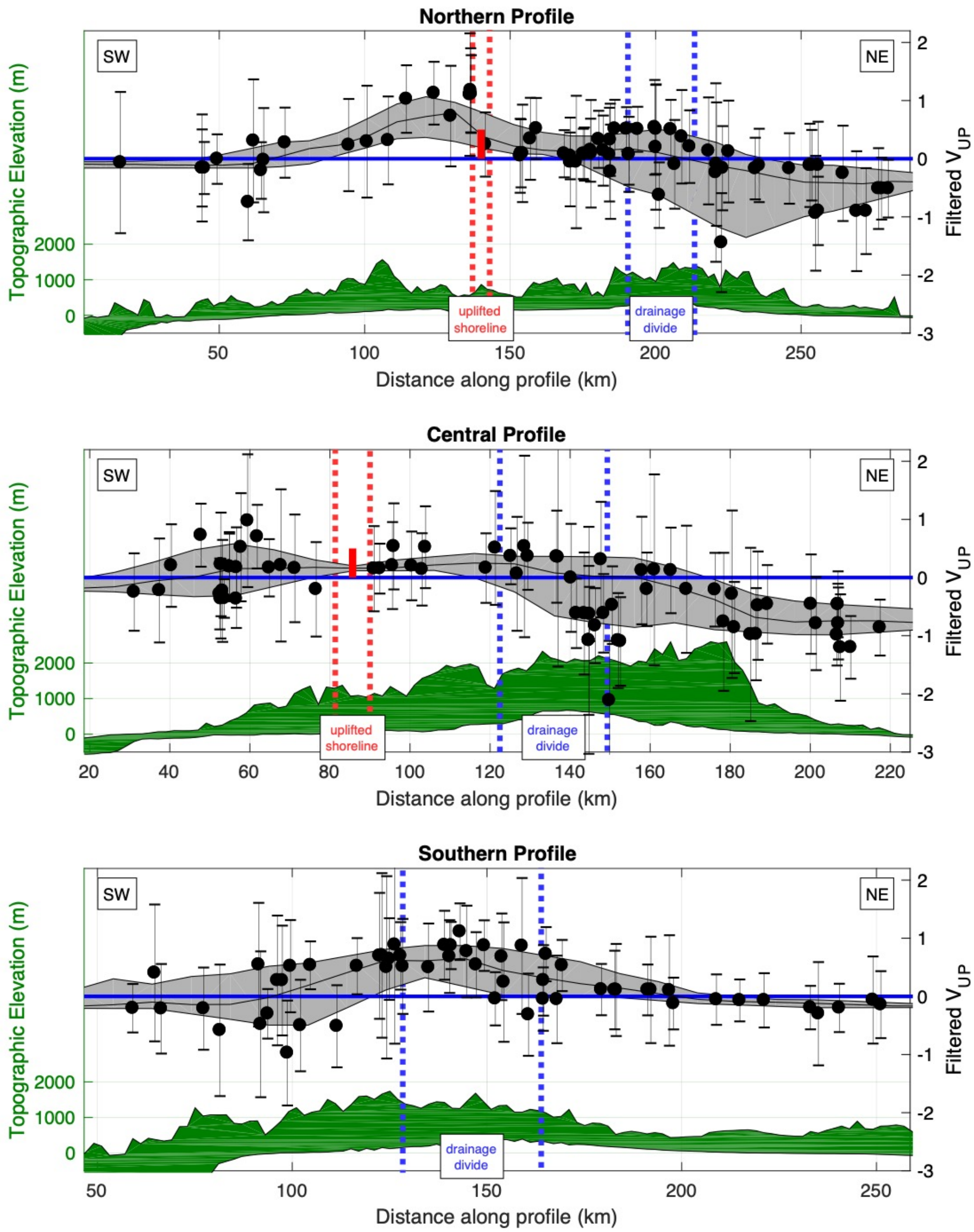

Figure 4. Profiles of vertical GPS velocity as a function of distance across three profiles whose locations are shown in Figures 1 and 3, where top is northern, middle is central, and bottom is southern profile. Black circles are values of median filtered GPS velocities and error bars with their 1-sigma uncertainties. The gray band behind indicates a smoothed envelope of the GPS Imaging vertical rate field, with the black line showing its median value within the profile rectangle. The green profile beneath the GPS values indicates the envelope of minimum to maximum elevation across the profile. The location of the drainage divide is shown with vertical blue dashed lines. The location of the Early Pleistocene uplifted shoreline (D'Agostino et al., 2001b) is indicated with a vertical short red bar whose length corresponds to the range of rates between 0 to 0.5 mm/yr. The dashed red lines indicate the extent of the shoreline within the profile rectangle.

Figure 5.

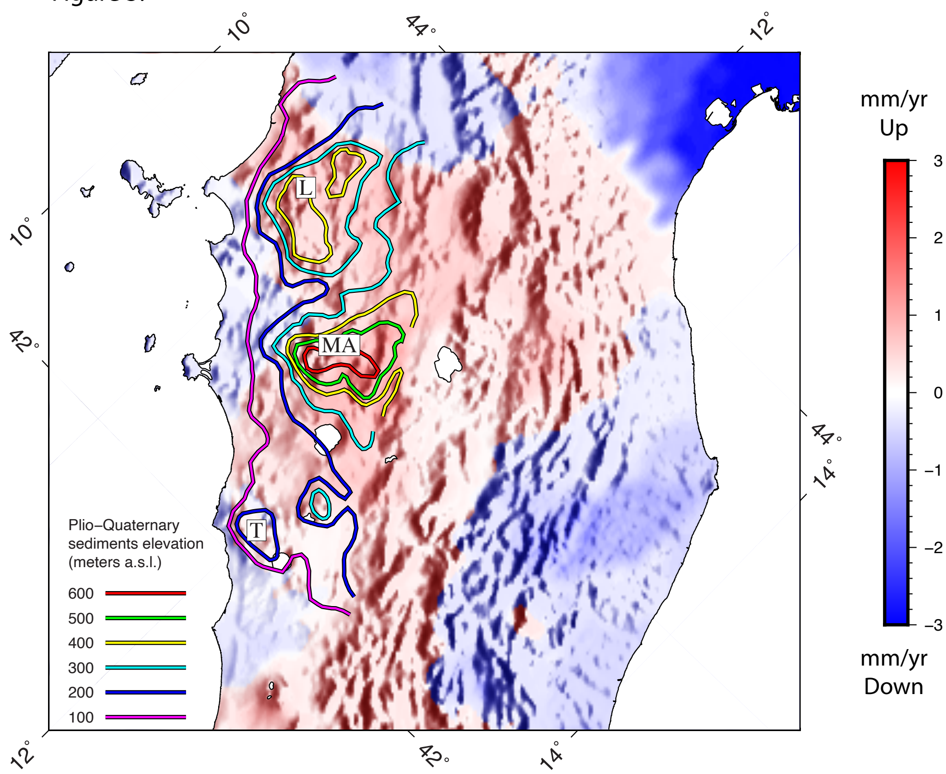

Figure 5. GPS imaging of vertical velocity field (same as Figure 3) and contours of elevation of Neogene marine sediments (Lower Pliocene-Quaternary) from Marinelli et al. (1993) showing the correlation between the vertical geodetic signal with regions of long-term Neogene vertical land motion and geothermal fields characterized by Quaternary magmatic intrusions (L, Larderello; MA, Monte Amiata; T, Monti della Tolfa).

Figure 6.

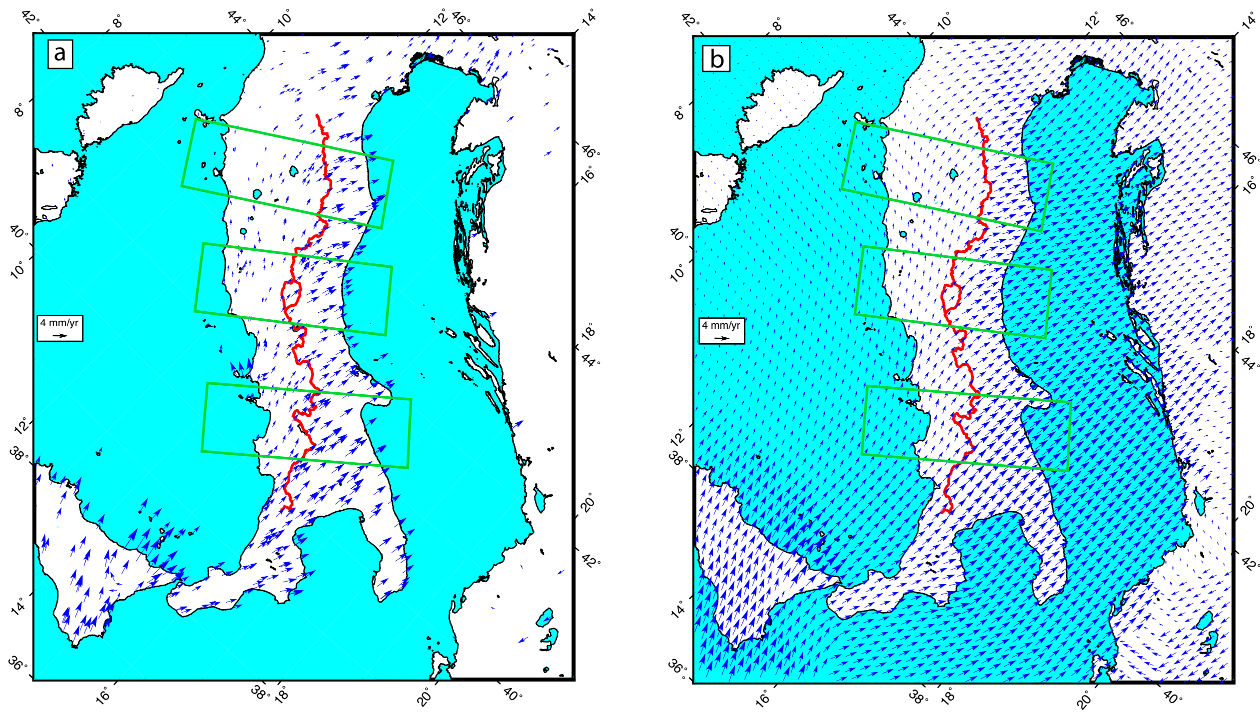

Figure 6. a) Median spatial filtered horizontal MIDAS GPS velocities from GPS time series in Eurasian reference frame. b) Gridded horizontal GPS velocity obtained using GPS Imaging. Other map elements are the same as in previous figures.

Figure 7.

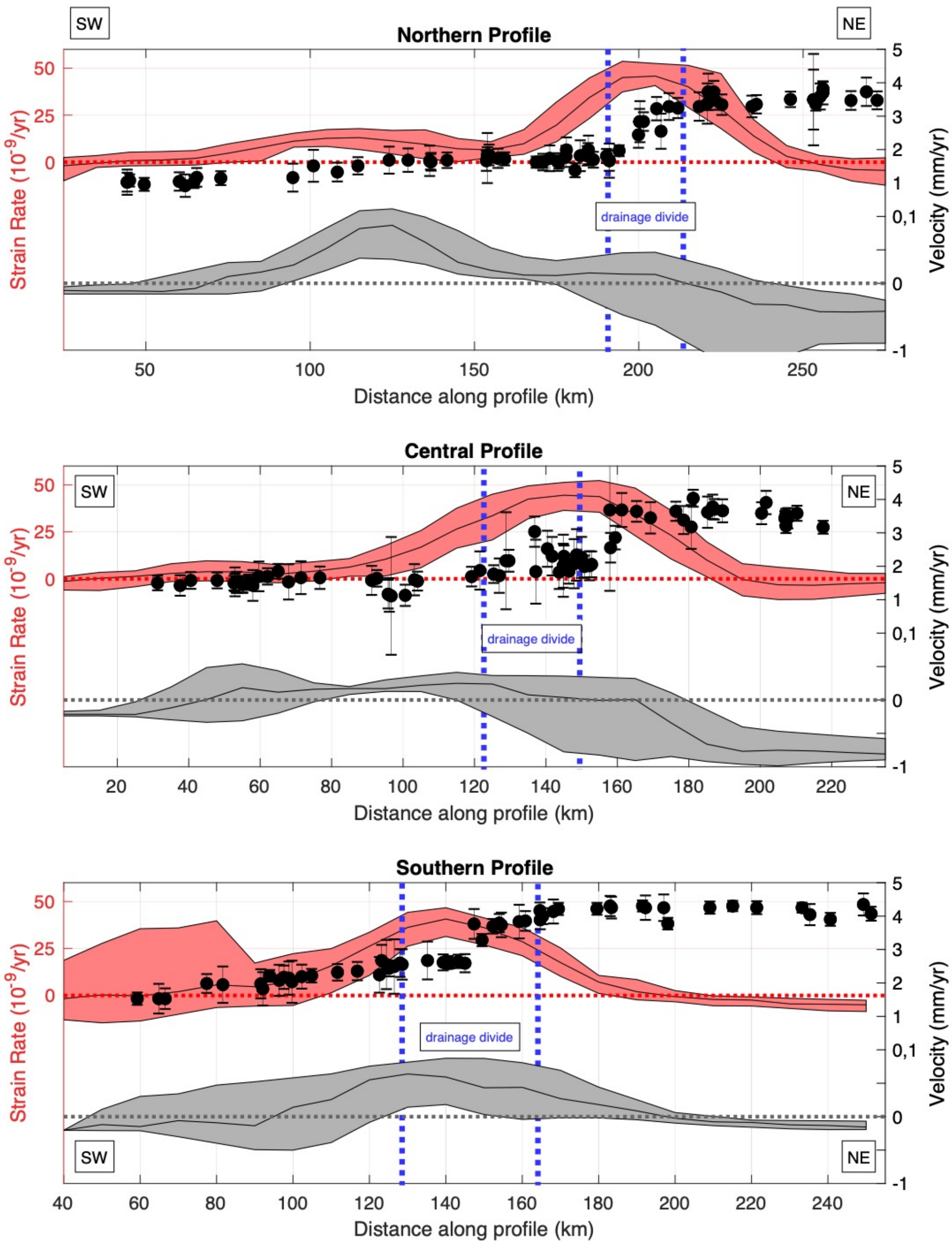

Figure 7. For same profiles shown in Figure 4, black circles indicate magnitude of median spatial filtered GPS velocity with 1-sigma uncertainty bars. Salmon color indicates smoothed envelope of dilatational strain rate estimated from gridded horizontal velocity field shown in Figure 6. The gray band indicates the same smoothed envelope of the vertical rate from Figure 4, with the black line indicating its median value. The location of the drainage divide is shown with vertical blue dashed lines. The horizontal dotted salmon and gray colored lines indicate zero strain rate and vertical rate, respectively.

Figure 8.

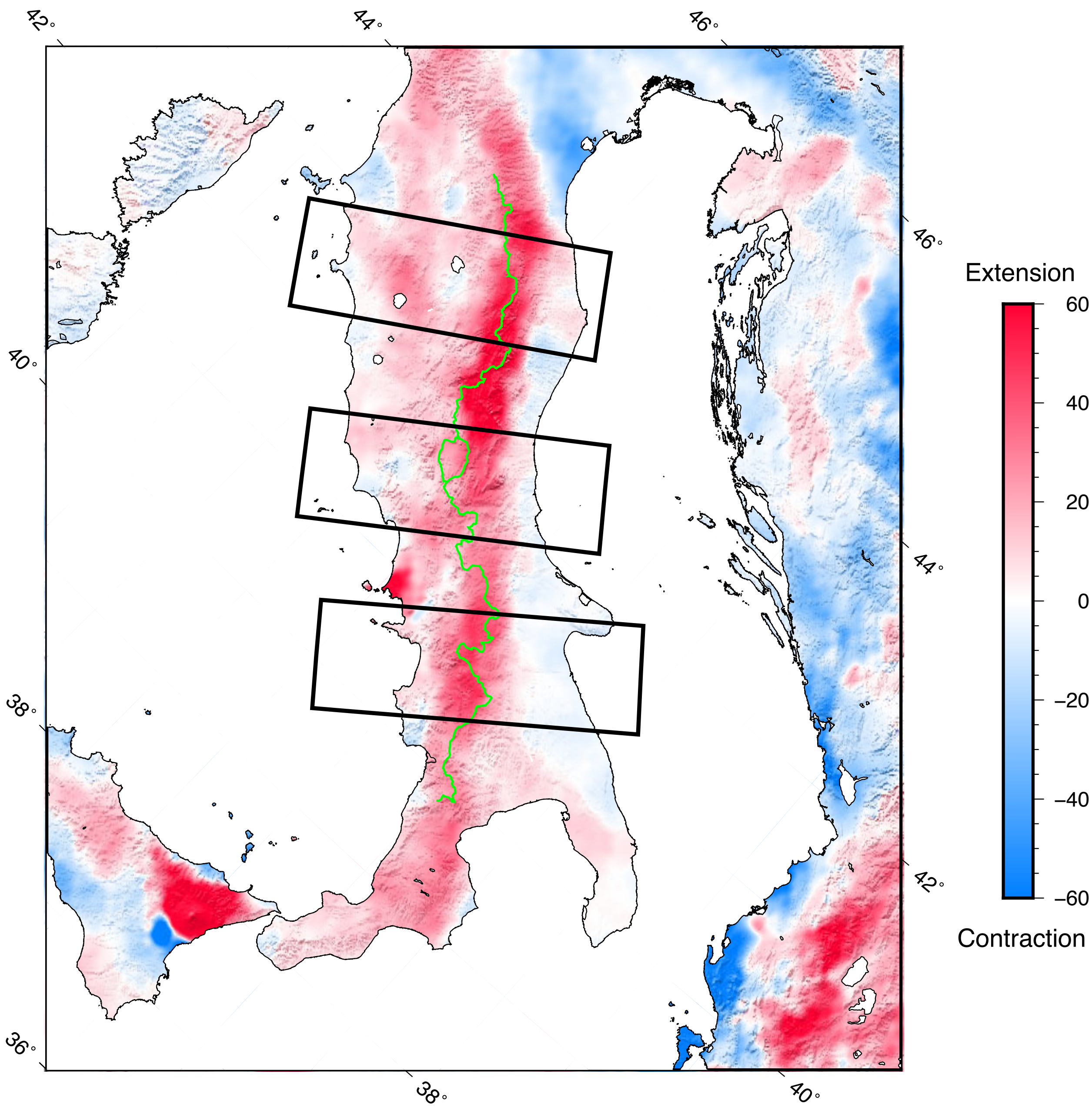

Figure 8. Map of dilatational component of strain rate derived from horizontal velocity field using GPS Imaging and a Gaussian averaging window of width w = 8 km (see supplemental materials). Color scale indicates value of strain rate in units of nanostrains/year, extensional in magenta color, contraction in cyan. Green line is drainage divide as in previous map figures.

Figure 9.

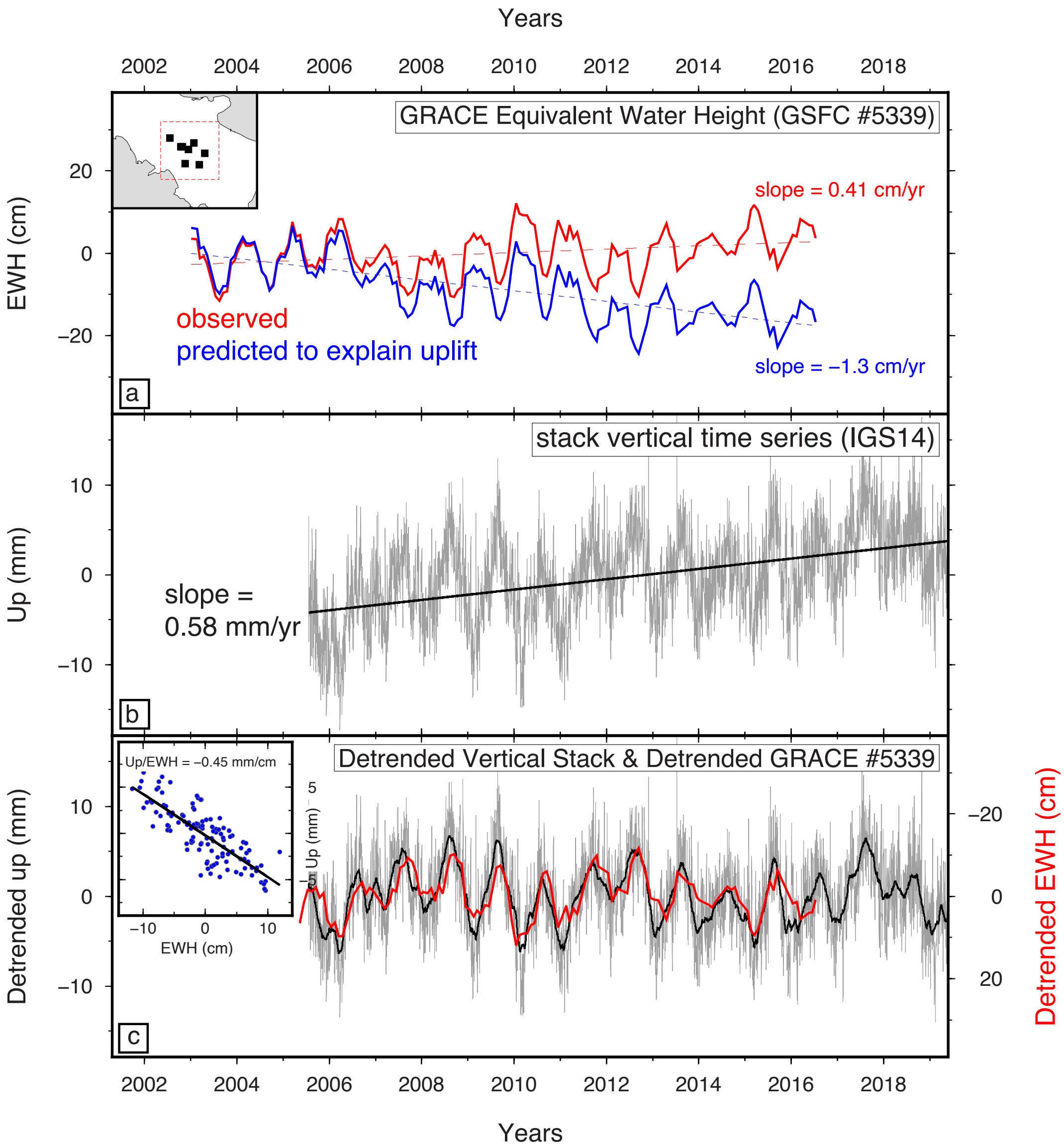

Figure 9. Analysis of hydrological forcing. a) Monthly equivalent water height (EWH) time series from GRACE (GSFC solution mascon #5339). The red line is the observed value together with the best-fit trend (dashed) showing weak increasing water loading. The blue line shows the same time series after detrending and addition of the trend required to explain the observed uplift in the case of hydrological loading. The inset shows the geographical location of the mascon. b) Stack of selected GPS vertical time series (stations shown in the inset of a)) and associated best-fit trend showing mean uplift rate of 0.58 mm/yr. c) Comparison between the detrended GRACE EWH observations (red) and detrended stacked vertical GPS positions (resampled at GRACE observation times, in black). The inset shows the regression between vertical displacement (Up) and EWH, giving a relation of -0.43 mm uplift per cm of EWH. This relation was used to calculate the predicted hydrologically-driven uplift rate shown in a), (see text for details). The disagreement of trends in a) illustrate that Apennine uplift is not attributable to hydrological loading.

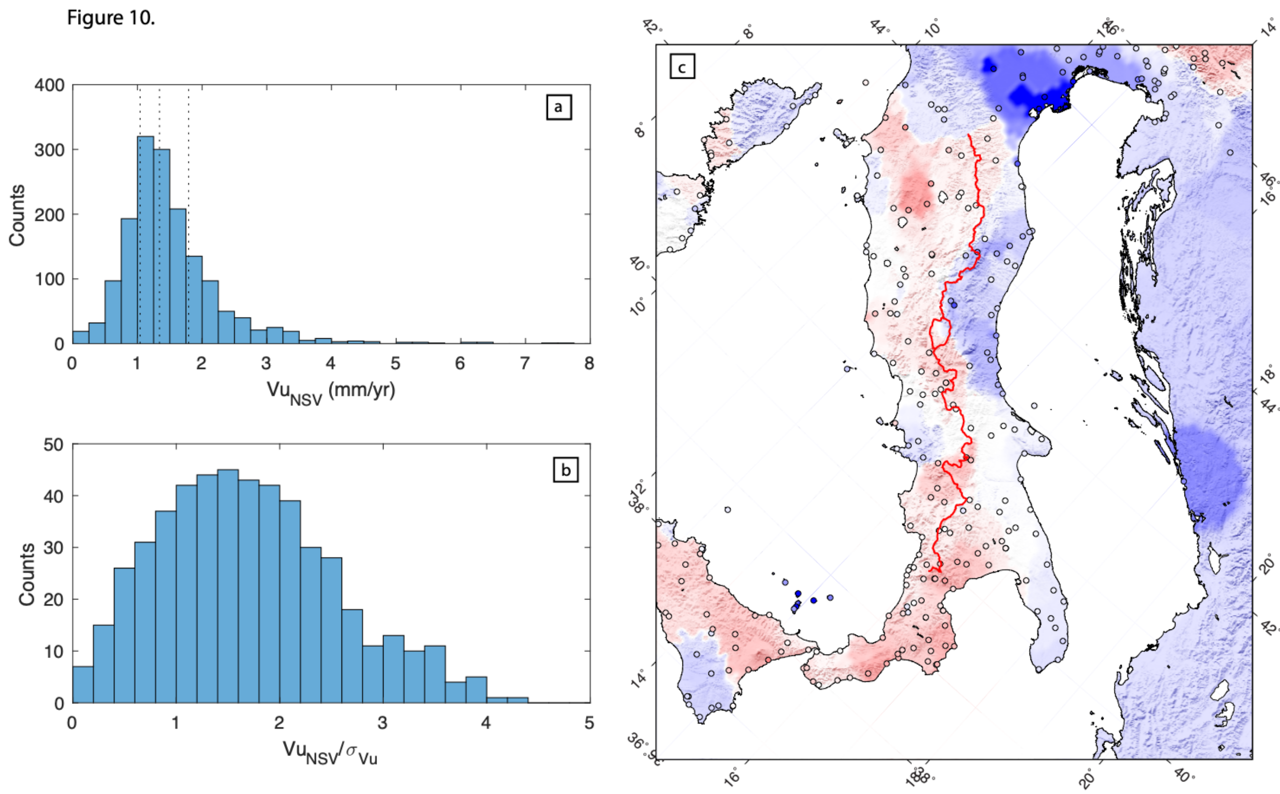

Figure 10. a) Histogram of vertical velocity variability index $V_{u,NSV}$. Vertical dotted lines indicate 25th, 50th, and 75th percentiles of the distribution. b) Histogram of the vertical velocity variability index divided by the uncertainty in the MIDAS vertical rate ($V_{u,NSV}/\sigma_{Vu}$) indicates a minority of velocities are have variability that is significantly different than the MIDAS rate. c) GPS Imaging of vertical velocity using only the subset of velocities that have variability below the median value of $V_{u,NSV}$ = 1.8 mm/yr.

Figure 11.

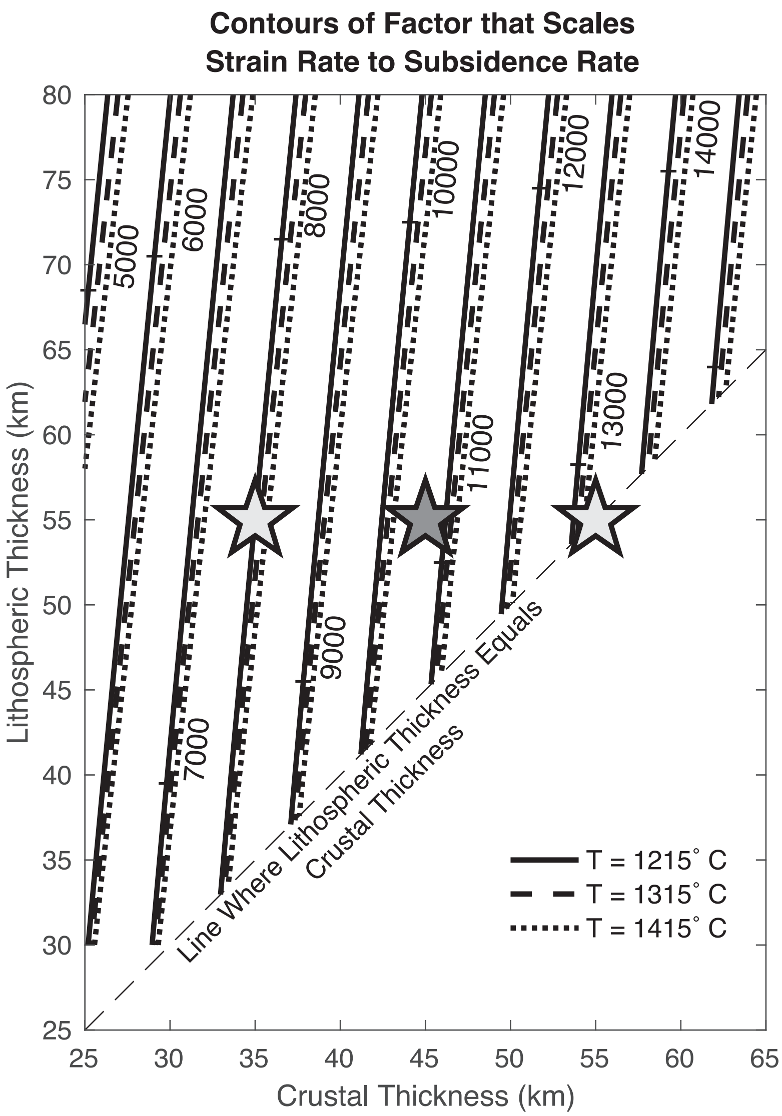

Figure 11. Contours of the scale factor predicting vertical subsidence rate expected from a given dilatational strain rate. The factor is calculated using equation (2) from Howell et al., (2017) for various values of crustal (t_c) and lithospheric (t_l) thickness and asthenospheric temperature T_l (see text for details). Grey stars indicate value for t_c = 35, 45 and 55 km and lithospheric thickness t_l = 55 km.

Figure 12.

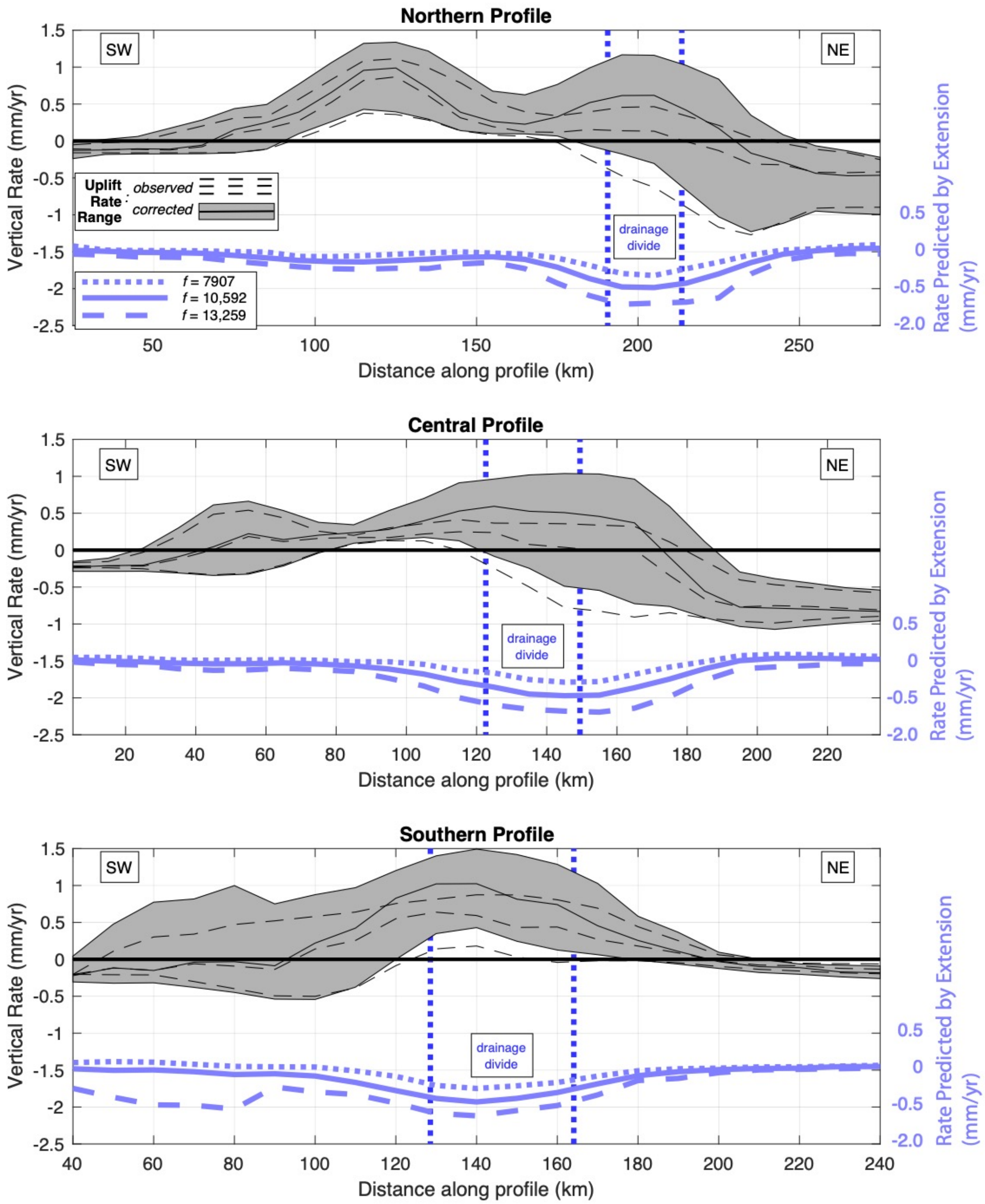

Figure 12. Estimated vertical rate of the mantle upwelling beneath the Apennines. We correct the imaged vertical rate field (dashed black lines are from Figure 4) for the rate expected from subsidence associated with crustal extension. For the same profiles as in previous figures, we use the scale factors of *f*=7907, 10,592, and 13,259 (from the location of stars in Figure 11) to predict the subsidence rates (dotted, solid, dashed purple lines respectively) from the geodetically observed dilatational strain rate. The predicted subsidence (negative vertical rate) is subtracted from the observed uplift rates so the corrected uplift rates (gray solid area) are greater than the uncorrected rates. Legend in a) applies to b) and c) as well.

Figure 13.

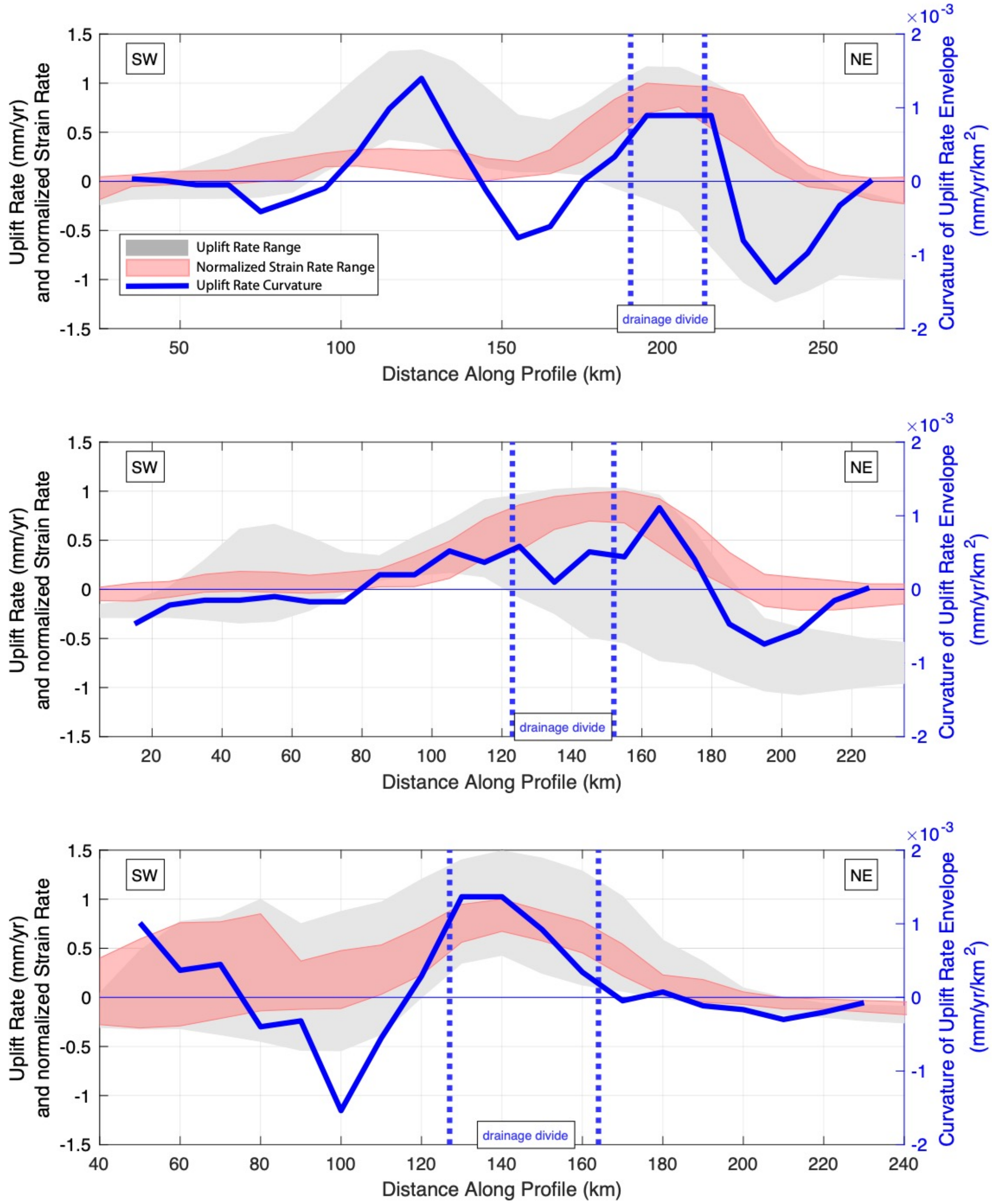

Figure 13. Median filtered profile of curvature (blue) of the uplift profile calculated with double finite difference of the uplift envelope. The sign has been changed so concave downward uplift signal curvature is shown with as positive second derivative. The uplift envelope (gray) is adjusted for thinning of the crust (Figure 12), and the strain envelope (salmon color) is from Figure 7. Location of drainage divide is shown as in previous figures.

Journal of Geophysical Research - Solid Earth

Supporting Information for

GPS Imaging of Mantle Flow-Driven Uplift of the Apennines, Italy

by

William C. Hammond[1] and Nicola D'Agostino[2]

1) Nevada Geodetic Laboratory
Nevada Bureau of Mines and Geology
University of Nevada, Reno
whammond@unr.edu

2) Istituto Nazionale di Geofisica e Vulcanologia
Osservatorio Nazionale Terremoti
Rome, Italy

Contents of this file

Supplementary Text
Supplementary Figures S1 to S6

Additional Supporting Information (Files uploaded separately)

Supplementary Table S2 - GPS velocities and uncertainties

Supplementary Table S1 - Networks and internet sites from which we obtained RINEX data

Introduction

The supplementary materials provide detailed information about parts of the GPS data analysis. Specifically, the correction for glacial isostatic adjustment, the estimation of the spatial structure function that is needed for GPS Imaging, and resolution tests of the GPS Imaging of vertical velocity. A separate file contains supplementary Table S1. This table contains the GPS velocities which are the main product of the GPS data processing and MIDAS estimation and are the underlying data for the GPS Imaging analysis presented in the main text and figures.

Supplemental Materials

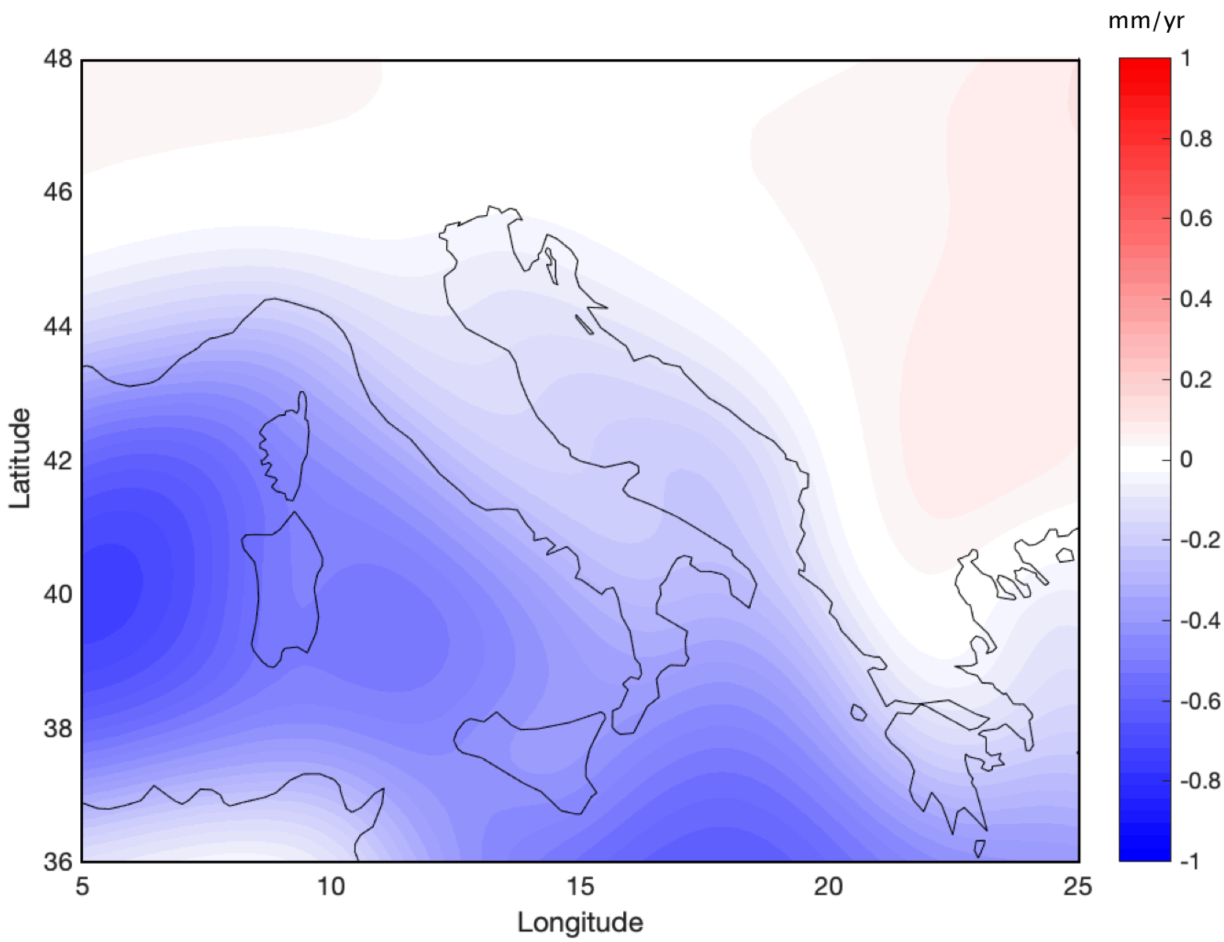

Supplementary Figure S1. Prediction of vertical geodetic velocity from ICE-6G model (Peltier et al., 2015, obtained from https://www.atmosp.physics.utoronto.ca/~peltier/data.php) used as a correction for vertical velocities estimated from GPS. Note color scale is different from that used in figures in main text in order to better highlight the gradients in vertical velocity. The scale in this figure extends from -1 mm/yr downward (blue) to +1 mm/yr upward (red).

Estimation of the Spatial Structure Function

We derive the spatial structure function (SSF) needed for the GPS Imaging analysis from the vertical GPS velocities as described in *Hammond et al.,* (2016). This function is a statistical representation of how the similarity in values between pairs of stations decreases with distance, analogous to a semivariogram in kriging analysis, but estimated using a robust approach that is itself insensitive to outliers in the vertical velocity data. In our implementation an SSF always has value 1 at zero distance and value zero at distance 180 degrees (the maximum distance on Earth's surface) decreasing monotonically. The SSF we derive from our GPS velocity dataset falls to 0.5 at ~0.3 degree, and to under 0.05 at 1 degree, and therefore falls off faster with distance than the one obtained in Figure 4C of Hammond et al., (2016) for the California and Nevada region. This indicates that the horizontal length scales in the vertical rate field for the Italian Peninsula are on average shorter than those in California and Nevada. Supplementary Figure S1 illustrates the stages of the generation of the SSF, its caption describes the

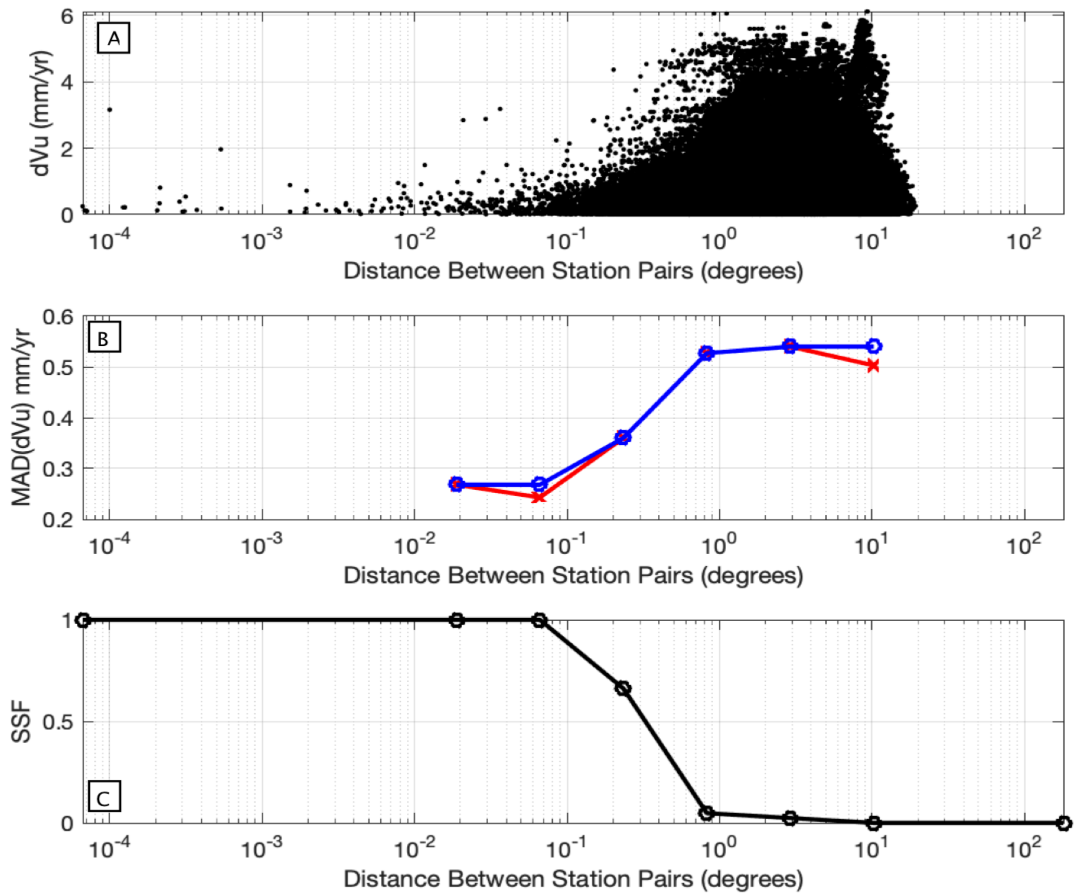

Supplementary Figure S2. Derivation of the SSF used in the GPS Imaging analysis. A) Scatterplot of the absolute value of the difference in median spatial filtered vertical GPS velocities as a function of distance between all pairs of stations within the domain shown in Figure 3. B) The median absolute deviation (MAD) of the differences in vertical velocity (red) for groups of rate differences inside bins centered at the data points indicated by 'x' and 'o' symbols. Larger values indicate greater spread of rates within the bin. Blue is the same curve except that the value at each point is the maximum of the red value and the previous value to enforce the SSF to be monotonically increasing. C) SSF function derived from the blue function (z) where SSF = (max(z) - z)/max(z) and then padded with a 1 at the beginning and a zero at the end.

Tests of Stability of GPS Imaging Vertical Rate Results

We assess the stability and repeatability of the GPS Imaging results by performing a sequence of tests using various subsets of the data. We divide the data into several different subsets and repeat the imaging using the same method used to generate Figure 3. Because some stations show significant variability in the vertical rates over multi-annual periods (e.g. Figure 10) the rates obtained may be sensitive to the time period over which they collect data, especially for stations with shorter durations between first and last observation.

In Figure S3 we show the results of dividing the data into three different time intervals. For each time interval we take the part of the GPS time series that lies within the indicated interval and use the station if the truncated time series is at least as long as the duration cutoff used in Figure 3 (2.5 years). The time intervals used are 2005.0 - 2012.0, 2008.0 - 2014.0, and 2012.0 - 2019.0. The first and last intervals are non-overlapping. We apply the MIDAS algorithm to the resulting truncated vertical component GPS time series to obtain the rates in each time period. Station coverage is not identical in all time periods owing to the installation or deactivation of some stations. A station can appear in more than one image if its time series is long enough to have at least 2.5 years in more than one time interval. While some details vary from image to image, the main features in the uplift signal, including uplift along the Apennines, Calabria and northern Sicily are present in all three images and have similar amplitudes. This indicates that the main features of the uplift and subsidence signals are not highly time variable. The greatest differences are in the Dinaric Alps east of the Adriatic Sea, where GPS station coverage is least complete.

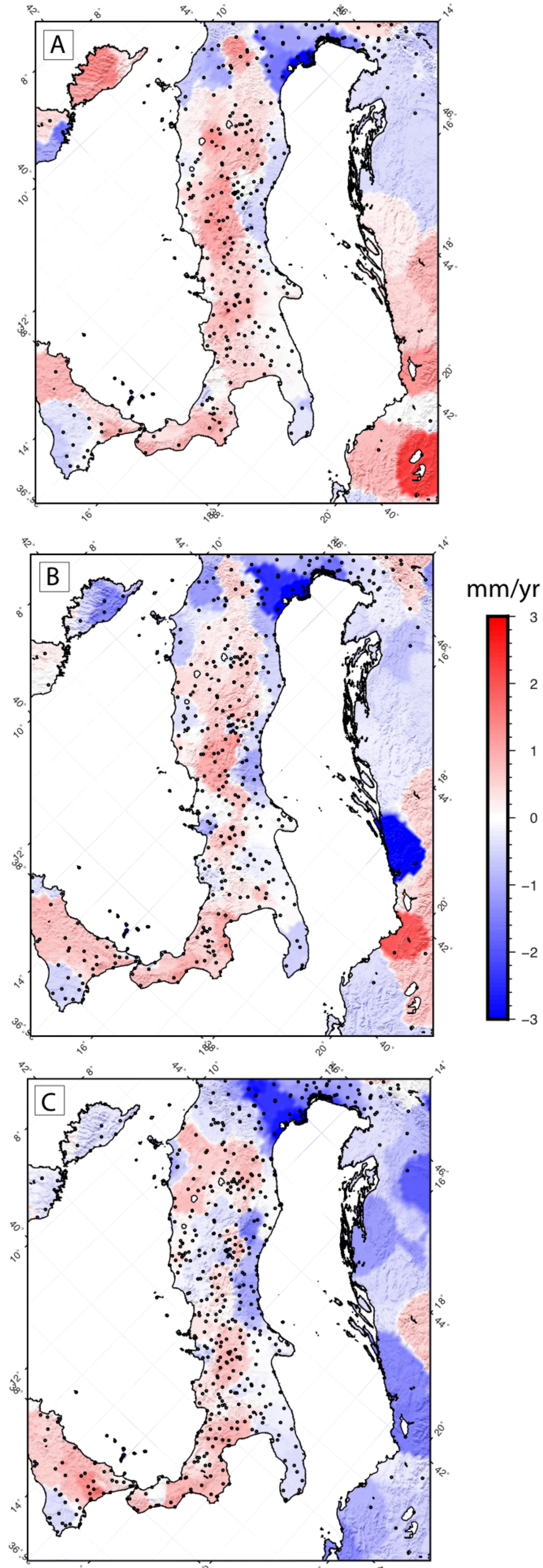

Supplementary Figure S3 (right). Results of GPS Imaging applied to time intervals of A) 2005.0 - 2012, B) 2008.0-2014.0, C) 2012.0 - 2019.0. Black dots are GPS stations inside the time interval that were used to perform the imaging.

We next show the results of dividing the data into two randomly selected non-intersecting subsets, where every station is in either one set or the other with no overlap. This selection tests whether the spatial coverage of GPS stations is redundant with respect to the signals of uplift we discuss. Selection of stations is done quasi-randomly by sorting stations by distance from the geometric center of the figure bounds, and then taking odd numbered stations as one set and even numbered stations as the other. This ensures that each subset has roughly the same number and same geographic coverage, and that differences in the imaging result are attributable to noise related to station coverage. The result, shown in Supplementary Figure S4, indicates that most of the long wavelength signal is consistent between the two figures, including along the length of the Apennines, Calabria and Sicily. Some minor differences are apparent, including in the central Apennines. The degree of difference between the two images based on the even/odd halves of the data is similar to the degree of difference between the separate time periods discussed in Supplementary Figure S3 above. This suggests that the spatial density of stations is approximately as important as the temporal duration of GPS coverage in the imaging. In each case using half the data provides an image that is approximately correct but is improved by including the addition of the other half. As in the test of different time periods the differences are greatest in the Dinaric Alps region where GPS station coverage is weaker.

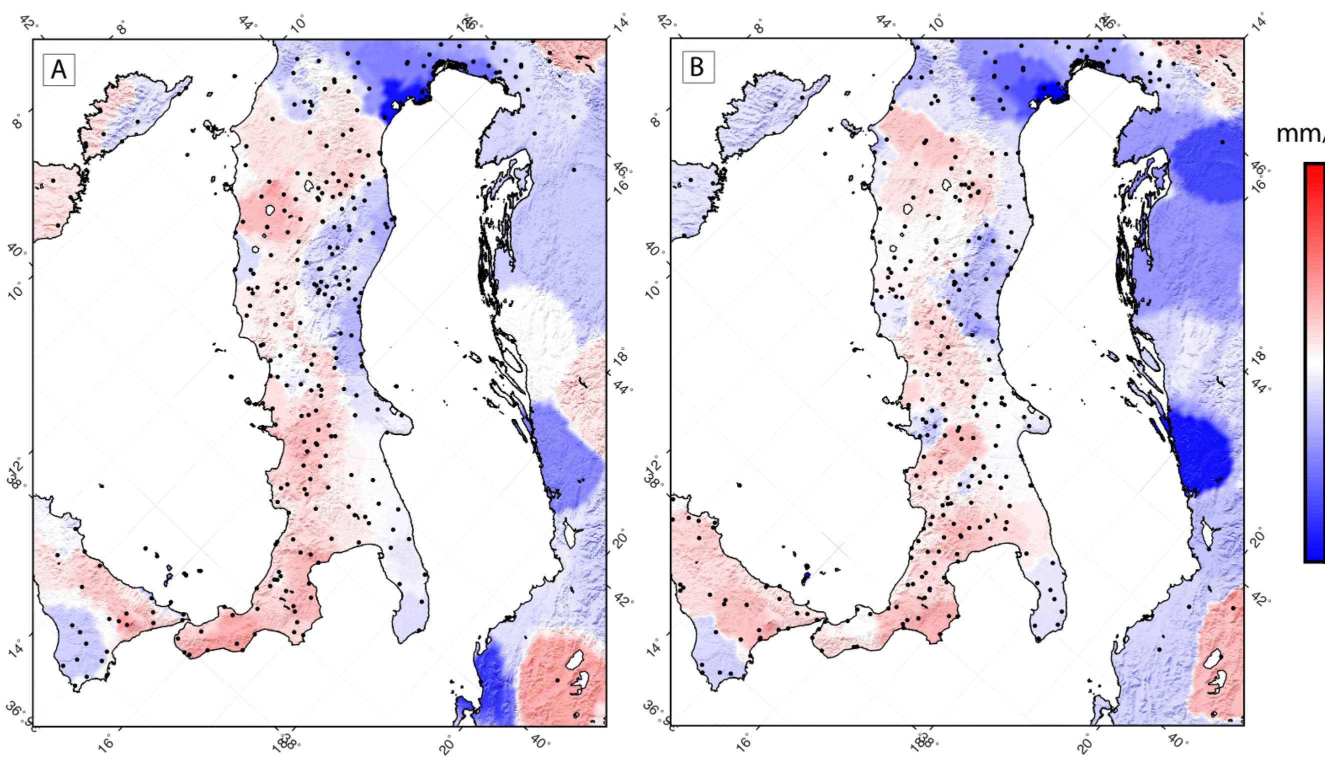

Supplementary Figure S4 (above). A) GPS Imaging of vertical rate using the even numbered stations when sorted by distance from the figure center. B) GPS Imaging usin the odd half of the stations.

Our third test varies the cutoff in minimum time series duration used for the imaging. Shorter duration time series are more prone to bias from multiannual vertical rate variability. Thus, we expect that imaging based on shorter duration time series to be less reliable owing to the interval sample bias, in addition to the higher aleatory uncertainty inherent to estimating trends from short time series. Since network coverage increases over time the inclusion of shorter time series could conceivably cause a temporal bias similar to the tests of different time series intervals detailed above. However, allowing shorter duration time series supplements the spatial coverage, and while they may introduce noise in the imaging, GPS Imaging exploits the power of numbers to find the median signal. This test illustrates the value of including shorter duration time series as opposed to restricting the analysis to only a sparser network of long-observing stations.

Supplementary Figure S5 shows the result in A) of imaging with only stations having 10 or more years of time series duration, and in B) the result of imaging using only stations with between 2.5 years and 10 years duration. The 10-year cutoff was chosen so that there are a similar number of stations in the two subsets, however these subsets to not have the same geographic distribution. The imaging results shows that for longer duration time series, the vertical rate field is similar to the field obtained using all the data (Figure 3), with uplift over nearly the entire length of the Apennines, Calabria and northern Sicily, though misses some of the uplift in the Larderello and Monte Amiata regions. The image obtained using only shorter duration time series has uplift in the northern Apennines and Calabria, but is missing uplift in the Central to Southern Apennines. This suggests that having a broad and dense distribution of GPS stations with long observation histories (>10 years data) is essential for resolving the signals of geographically coherent vertical uplift in the Apennines, but also it benefits substantially from the introduction of relatively new stations with shorter duration time series.

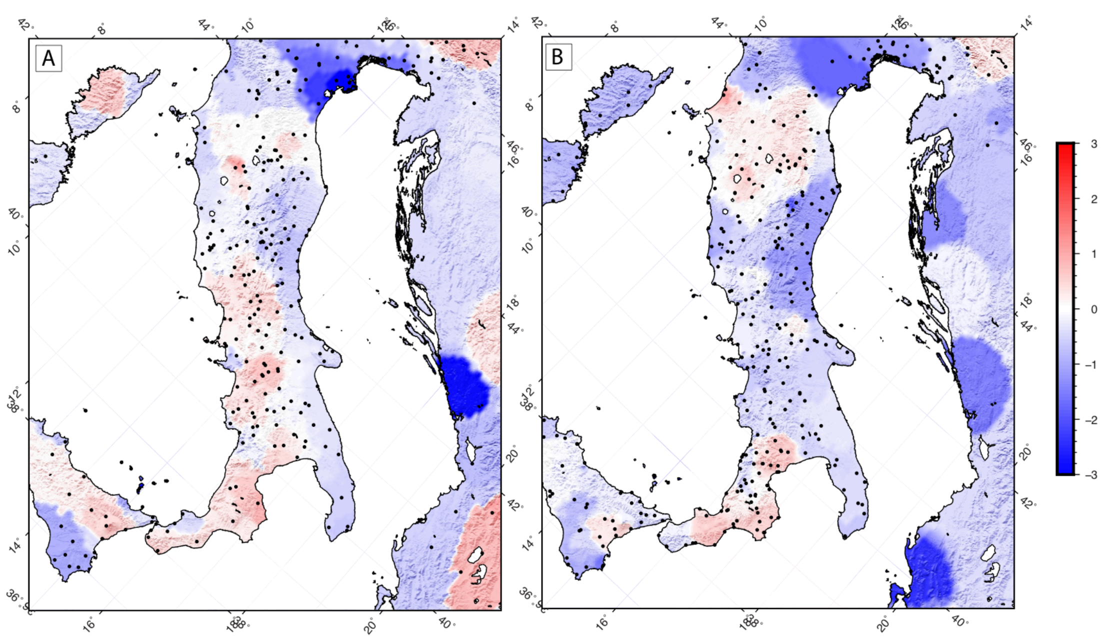

Supplementary Figure S5. GPS Imaging using A) only stations with 10 years or greater duration time series and B) only stations with between 2.5 and 10 years duration time series.

Regularization of strain rate

In our GPS Imaging of horizontal tensor strain rates described in the main text we estimate velocity gradients over a finite distance which we must choose a priori. The choice of horizontal strain length scale (*w*) has an effect on the degree of smoothness and misfit to the data. As in all strain mapping analyses, a longer length scale tends to create a smoother and simpler variation of estimated strain rate with a smaller overall model norm, greater data misfit, but greater certainty in individual strain rate estimates at grid points. In order to find a model with both low misfit and low uncertainty we perform our strain rate estimation using test values of *w* from 2 to 20 km, stepping at 2 km intervals. For each model we compute the mean and median of the weighted sum of residuals to represent misfit between the data and model predictions. To represent the model norm we calculate the root-sum-square of each strain rate component (dilatation, shear and magnitude of strain rates). Figure S6 shows the model misfit and norms as a function of *w* in km. The results show that model norms decrease and model misfits increase with increasing *w*. In the text we present a model with value of $w = 8$ km since this the rate of reduction in model norm begins to decrease substantially, and this value the model misfit begins to climb rapidly.

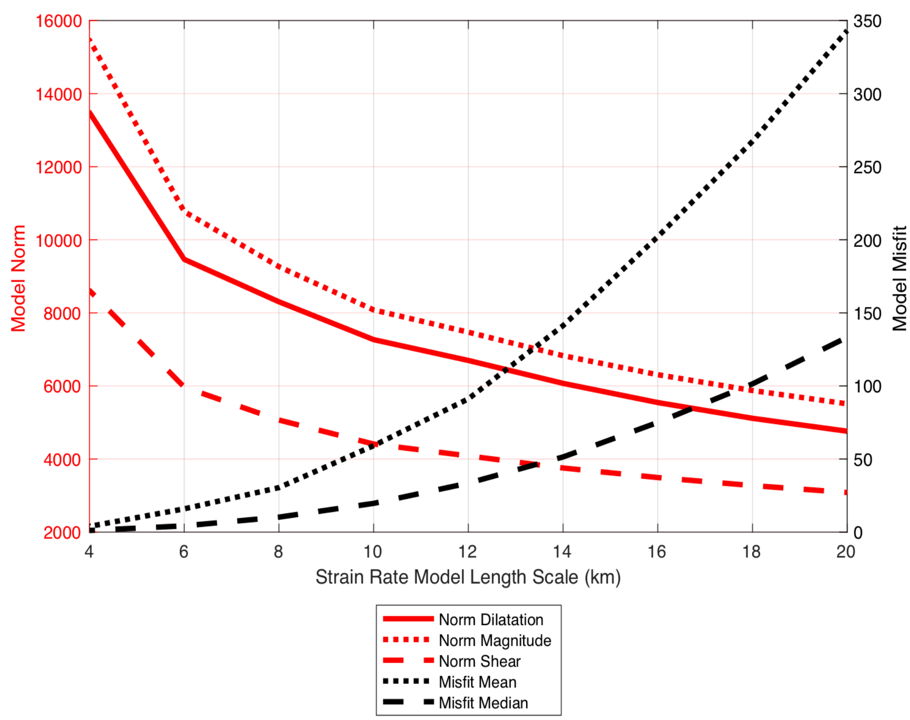

Supplemental Figure S6. Model misfit and model norm as a function of strain rate length scale parameter *w* in km.